

Decoding Local Field Potential Oculomotor Signals During Reach Planning for Neural Prosthetic Systems



Brendan Thorn

Department of Electrical, Computer, and Software Engineering

Faculty of Engineering

McGill University

Montreal, Quebec, Canada

July 2016

A thesis submitted to McGill University in partial fulfillment of the requirements of the degree
of Master of Engineering

© Brendan Thorn 2016

This thesis is dedicated to my parents, George and Becky Thorn.

Thank you for everything.

Acknowledgements

The author acknowledges the partial financial support of an Alexander Graham Bell Canada Graduate Scholarship, awarded by the Natural Sciences and Engineering Research Council of Canada.

I would first like to thank my supervisor, Prof. Sam Musallam, for giving me the opportunity to study in the McGill Neural Prosthetics Lab. His knowledge and passion for science, as well as the trust and confidence he placed in me, will continue to have a profound impact on my life.

I am enduringly grateful to Dr. Greg Stacey for starting me on the right path, patiently answering my questions along the way, and still finding energy for greatly appreciated encouragement. I am similarly indebted to Prof. Erik Cook, along with his students, for welcoming me to weekly lab meetings, taking time to understand my work, and consistently providing timely wisdom.

My lab-mates Rubing Xu, Nathan Freidman, and Victor Lu made me feel welcome from my very first day at McGill, and they have all helped me emerge through the trials of research, thesis-writing, and life as a graduate student.

For help with thesis editing, I would like to thank Katrina van Draanen and Nolan Thorn; for help with translating the abstract, I would like to thank Alfred Kenny. Most of all, for their constant friendship, conversation, and inspiration, I am deeply grateful to each of them.

Finally, I would like to thank my family in Westbank for all of their love and support, Elizabeth Loggia and Kris Youakim for always helping me find the right perspective, and David Fallis and Jeanette Lesiuk, for being there in the beginning and every day since.

Contents

| | |
|-------------------------------------------------------------------------|----|
| Acknowledgements ----- | 3 |
| Abstract ----- | 6 |
| Abrégé----- | 7 |
| Contributions ----- | 8 |
| 1. Introduction----- | 9 |
| 1.1 Neural prosthetic systems ----- | 9 |
| 1.2 Overview ----- | 10 |
| 1.3 Review of related literature ----- | 12 |
| 1.3.1 Local field potential ----- | 13 |
| 1.3.2 Saccades and smooth pursuits ----- | 14 |
| 1.3.3 Cortical pathway for visually guided reaching----- | 15 |
| 1.3.4 Posterior parietal cortex ----- | 17 |
| 1.3.5 Pre-motor cortex ----- | 20 |
| 1.3.6 Motor versus cognitive control of neural prosthetic systems ----- | 21 |
| 1.3.7 Decoding algorithms ----- | 23 |
| 1.4 Objectives ----- | 25 |
| 2. Theory and methods----- | 28 |
| 2.1 Animal subjects, care, and surgical procedures ----- | 28 |
| 2.2 Electrophysiology and data acquisition ----- | 29 |
| 2.3 Behavioral task ----- | 30 |
| 2.4 Data analysis ----- | 31 |
| 2.4.1 Data pre-processing----- | 31 |
| 2.4.2 Multi-taper analysis----- | 32 |
| 2.4.3 Analysis of variance ----- | 34 |
| 2.4.4 ANOVA for direction classification----- | 36 |
| Table 1 ----- | 37 |
| 2.4.5 Naïve Bayes classifier----- | 38 |
| 2.4.6 ANOVA for onset detection----- | 40 |
| Table 2 ----- | 42 |
| 2.4.7 Support vector machine ----- | 43 |

| | |
|-----------------------------------------------------------------------|----|
| 2.4.8 Parameter optimization----- | 45 |
| 3. Results----- | 48 |
| 3.1 Decoding eye movement direction----- | 48 |
| 3.1.1 Directional tuning for eye movements in areas MIP and PMd ----- | 48 |
| 3.1.2 Predicting movement direction with naïve Bayes classifier----- | 51 |
| 3.2 Detecting eye movement onset----- | 53 |
| 3.2.1 Temporal tuning for eye movements in areas MIP and PMd ----- | 54 |
| 3.2.2 Detecting movement onset with support vector machine----- | 54 |
| 4. Discussion ----- | 58 |
| 4.1 Eye movement direction decoding----- | 58 |
| 4.1.1 Eye movement directional tuning----- | 58 |
| 4.1.2 Eye movement direction decoding ----- | 59 |
| 4.2 Eye movement onset detection ----- | 61 |
| 4.2.1 Eye movement temporal tuning----- | 62 |
| 4.2.2 Eye movement onset detection ----- | 63 |
| 5. Conclusions and neural prosthetic applications ----- | 66 |
| 6. Figures ----- | 68 |
| Figure 1 ----- | 68 |
| Figure 2 ----- | 69 |
| Figure 3 ----- | 70 |
| Figure 4 ----- | 71 |
| Figure 5 ----- | 72 |
| Figure 6 ----- | 73 |
| Figure 7 ----- | 74 |
| Figure 8 ----- | 75 |
| Figure 9 ----- | 76 |
| Figure 10----- | 77 |
| Figure 11----- | 79 |
| 7. References ----- | 80 |

Abstract

Using signals recorded from the brain to control an artificial device, neural prosthetic systems are a promising option for restoring independent motor control to people with permanent injuries, such as paralysis. Since humans generally look towards their target before reaching or moving, motor prosthetic applications could be improved with reliable decoding of eye position. For this thesis, we studied oculomotor signals encoded in the cortical local field potential (LFP) during reach planning. LFPs recorded from the medial intra-parietal (MIP) and dorsal pre-motor (PMd) areas of the brain – known to encode reach intentions in coordinates related to eye position – were transformed to the time-frequency domain using multi-taper analysis. We investigated whether LFP spectral power can be decoded for two novel purposes: i) to determine saccade or pursuit eye movement direction during a concurrent reach planning period; and ii) in the same reach planning scenario, to detect saccade or pursuit eye movements within a 100 ms post-onset period. First, using a naïve Bayes classifier, we showed that eye movement direction is encoded in LFP spectral power independently of reach direction; however, decode accuracy may be degraded by concurrent reach planning. Second, we proposed a causal, general support vector machine-based algorithm for detecting eye movement onset in real-time. We then implemented single-trial simulations to demonstrate its qualitatively desirable behavior. We showed false detections were clustered near the post-onset period and true positive detections were made at a significantly above-chance rate for saccades and pursuits. Our results suggest that MIP and PMd LFPs could potentially be used to decode oculomotor signals, and thereby improve reach-related neural prosthetic devices.

Abrégé

Des systèmes prothétiques neuronaux sont une option prometteuse pour rétablir le contrôle moteur indépendant aux personnes avec les blessures permanentes, telles que la paralysie. Dans cette mémoire, nous étudions les signaux oculomoteurs qui sont encodés dans le potentiel de champ local (PCP) cortical pendant la planification de portée. Les PCPs enregistrées des zones du cerveau sensorimoteur médial intra-pariéctal (MIP) et dorsale pré-moteur (PMd) - connus pour encoder les intentions de portée comme les coordonnées liées à la position de l'oeil - sont transformés au domaine temps-fréquence en utilisant l'analyse multi-effilage. Nous examinons si le PCP peut être décodé d'une manière fiable pour deux nouveaux objectifs: i) pour déterminer si la direction saccade ou poursuite peut être vérifiée près du temps de son commencement pendant qu'une portée instruite précédemment est prévue simultanément; et ii) dans le même scénario de planification de la portée, pour déterminer si les saccades ou poursuites peuvent être détectées dans les 100 ms avant le commencement du mouvement. Tout d'abord, en utilisant un classificateur de Bayes naïf, nous montrons que la direction du mouvement de l'oeil est encodée dans la puissance spectrale du PCP, mais la précision du décodage est sévèrement diminuée par la planification de la portée concurrente. Deuxièmement, nous proposons un algorithme qui est causal, général et basé sur un machine à vecteurs de support pour détecter le commencement des mouvements oculaires en temps réel de la puissance spectrale du PCP. Nous menons les simulations seules essaiées pour démontrer son comportement qualitativement souhaitable. Nous utilisons les données enregistrées des zones MIP et PMD pour montrer que les fausses détections sont regroupées de manière disproportionnée à proximité de la période de commencement et les taux de vraies détections positives sont considérablement au-dessus le hasard pour les saccades et poursuites. Nos résultats suggèrent que la puissance spectrale du PCP n'est peut-être pas un signal de commande porté-prothétique acceptable pour obtenir de l'information oculomoteur directionnelle; cependant, il peut être efficace comme source temps réel des informations temporelles liées à des changements dans l'état comportemental, et en particulier, l'apparition des saccades et des poursuites.

Contributions

All animal-related work and data collection was performed by Dr. Sam Musallam and Dr. Richard Greg Stacey. All writing and data analysis for this thesis was performed by Brendan Thorn.

1. Introduction

1.1 Neural prosthetic systems

When people lose sensory or motor capabilities, neural prosthetic systems provide a promising avenue for regaining independent functionality. Around the world, millions of people are afflicted with blindness, deafness, limb loss, ALS, and paralysis [1,2,3,4,5]. With such permanent conditions, there are few options for restorative treatments. However, by combining research and technology from fields like neuroscience, machine learning, and engineering, neural prosthetic systems have already helped people regain sensory and motor control.

The most successful sensory prostheses currently in use are cochlear implants (CIs). CIs are surgically implanted electronic devices that approximate the actual hearing process of humans. Roughly speaking, a microphone is used to record sound near the ear; the recorded sound is then processed, transformed into a frequency domain signal, and, after further bandpass filtering, is transmitted to an electrode array that has been inserted into the cochlea. Finally, a specified electrode on the array stimulates a corresponding set of naturally occurring auditory nerve fibers, leaving the patient's brain to finish interpreting the stimulus. CIs have been successfully implanted in hundreds of thousands of people in North America alone, with outcomes varying greatly from those with almost no improvement in hearing to congenitally deaf subjects who are able to attain nearly normal levels of oral communication [6]. Visual prosthetics are also being developed to provide vision to patients with severe or complete blindness. In general, these systems work by electrically stimulating the retina or other parts of the visual tract. A camera is used to capture input, the information is transmitted to an electrode device, and a representative but low-resolution light pattern is written to the nervous system. The Argus II retinal prosthesis became the first such system approved by the FDA in 2012 [7]; however, only minor improvements to vision have been attained from any visual prosthetic system so far.

More relevant for those suffering from conditions like ALS and paralysis are motor prosthetic systems. Many patients experience loss of motor capability due to nervous system damage below the brain stem. In other words, the motor commands generated by the brain are normal, but the

signal is corrupted, interrupted, or otherwise cannot be executed. Motor prosthetic systems use naturally generated neural commands by recording an appropriate part of the brain, processing the signal externally, and then applying the signal to control an artificial device. Several groups have shown that people can effectively control robotic limbs with this approach (e.g. [8,9]), and many other studies have reported successful brain-control trials with monkeys (e.g. [10,11]). This means the signal processing and control of motor effector (i.e. mouse cursor or robotic arm) are executed in real-time with no external guidance or input after the trial has begun. One recent study reported that signals recorded from the motor cortex of a tetraplegic 24-year-old male were decoded and used to control a custom device that stimulated muscles in his own arm [12]. He was then able to make movements composed of six independent motions, or degrees of freedom, between his wrist and hand, including accurate pinches and grasps. New applications of powerful machine learning algorithms, improved recording quality and bandwidth, as well as continued improvement in understanding reach and movement planning and execution, are leading to promising advances in motor prosthetic systems.

1.2 Overview

When humans plan and execute a reach, we most often look at our target first. Therefore, one way to improve the performance of motor prosthetics for reaching tasks is to also know where the subject is looking. While eyes are sensory organs, they are effective partially because of the way they move. Eye movements allow a person to keep their gaze centered at the locus of attention. This means that the central region of the retina, which is called the fovea and has the densest population of photoreceptive cells, stays focused on the target that a subject may want to reach towards. The oculomotor commands that drive these eye movements are generated, maintained, and updated by a system distributed throughout the cortex. This distributed nature means we can often infer eye position and movement intentions from brain activity at sites not directly related to the formulation of eye movements. In this study, we decoded eye movements using signals recorded from brain areas known for reach planning— the medial intra-parietal cortex (MIP) and dorsal pre-motor cortex (PMd) [11,13,14,15]. Because the amount of independent information that can be simultaneously extracted from neural recordings is one of

the rate limiting factors in prosthetics research, obtaining an additional information stream from data that is already used could improve performance.

Early neural prosthetic studies used either electro-encephalograms (EEGs) or micro-electrode probes to record neural activity. The former captures extremely low-amplitude electric potential – or voltage – signals from electrodes placed on the subject’s skin, while the latter records action potentials – commonly known as spikes – from a small number of neurons in its immediate proximity. Consequently, the voltage and the spike counts would comprise the control signal for the prosthetic systems. While EEGs provide a sustainable and non-invasive signal, recording across the skull greatly diminishes the attainable level of spatial resolution, dampens the signal, and introduces noise. Single- or multi-unit (neuron) spike recordings avoid these problems, but require invasive surgery. Further, on the timescale of months, spike recordings begin to deteriorate in amplitude and quality due to scar tissue buildup and other biological responses [16,17]. Although new probe designs and advanced materials are being developed to mitigate these effects, effective spike recording beyond the order of five years is only beginning to become possible [18]. To avoid some of the issues presented by EEG and spike recordings, we used a less studied, yet very promising, control signal.

The local field potential (LFP) is a low-pass filtered version of the raw electrophysiological voltage signal that is recorded with probes implanted in the cerebral cortex. It reflects an extracellular summation of electrical activity occurring within a relatively extended region surrounding the probe, called a listening sphere. This region can range from tens of microns to several millimeters in radius, depending on factors like brain area and recording hardware [19,20]. And while the LFP is recorded with the same probes or arrays as spikes, it is more robust to scar tissue buildups and slight position changes because it does not require close proximity to any specific cell. These factors make the LFP a more durable signal than spikes without conceding signal quality and resolution to the extent of EEGs [21,22]. As such, the LFP is an attractive candidate prosthetic control signal. A deeper review of LFP attributes, drawn from the literature, is provided in 1.3.1.

In this thesis, we summarize our investigation of LFPs recorded from MIP and PMd. Each recording occurred during a short time interval that included a single eye movement, which was executed while a previously instructed reach was being planned (see 2.3 for description of the behavioral task). We used two classification algorithms – a naïve Bayes classifier and a support vector machine (see 2.4.5 and 2.4.7) – to simulate real-time decoding of eye movement direction and onset time, respectively. By demonstrating that such oculomotor variables can be decoded from reach-related brain areas, while a reach is simultaneously being planned, we established LFPs from MIP and PMd as a source of information that can potentially be used to improve motor prosthetic performance.

In section 1.3, we provide the scientific foundation for this study through a review of related literature, and in section 1.4, we outline the specific objectives. In chapter 2, we detail our experimental methods, along with the corresponding theory.

1.3 Review of related literature

In this review, we characterize the signal processing and neurological basis for the local field potential (1.3.1), briefly discuss saccade and smooth pursuit eye movements (1.3.2), and outline the cortical areas involved in visually guided reaching (1.3.3), with emphasis on areas MIP and PMd (1.3.4-1.3.5). We then compare traditional motor prosthetics with the competing idea of cognitive neural prosthetics (1.3.6), and finish with an overview of commonly used decoding algorithms (1.3.7).

Studies referenced throughout this review heavily rely on non-human primate (NHP) subjects – especially macaque monkeys. As such, they necessarily rely on the analogous nature of the human and NHP visual and reach planning systems. While some anatomical labels may, therefore, be specific to macaque neurophysiology, a homologous area is almost always well established. A great deal of evidence has been gathered to justify this assumption (e.g. [23,24]), and such evidence provides the scientific basis for using NHP subjects as human surrogates.

1.3.1 Local field potential

As noted in section 1.2, the local field potential is the oscillatory and relatively slowly varying component of the extra-cellular voltage signal recorded by cortical probes or subdural electrode arrays. Measuring these signals is possible due to the constant electro-chemical communications between neurons. Neurons can be thought of as basic cellular units in the massive parallel computing structure of the brain – estimates suggest an adult human brain contains on the order of 10^{11} neurons [25]. On a coarse and generalized level, neurons are composed of a possibly large number of dendrites that connect to the soma - which contains the cell's nucleus - as well as a single axon that extends away from the soma and ends at the axonal terminal, off of which multiple synapses branch. When the dendrites collectively receive enough stimulation from other neurons to reach a positive voltage threshold, the soma fires an action potential – a large, non-linear electric impulse – down the axon. As the spike propagates to the axonal terminal, the synapses are activated to make excitatory or inhibitory electro-chemical interactions with the dendrites of other neurons. When a spike signal is recorded, it is usually the action potentials from large pyramidal cells that are measured. In contrast to spikes, LFPs are thought to primarily capture the combined synaptic activities of nearby neurons, although the exact sources of the signal are somewhat unknown [26,27]. Oftentimes, synaptic activities do not aggregate in excess of the potential threshold that produces a spike; however, the LFP is sensitive to these inputs nonetheless. This additional information can be construed as a positive feature of the LFP that is not captured by the spike signal.

The LFP has several other appealing properties. First, it is easily isolated by low-pass filtering the raw voltage signal, usually with a cut-off frequency at or below 500 Hz [28], thus attenuating the spike and high frequency noise portion of the signal. Second, due to its lower frequency nature, studies have shown that, relative to spikes, it correlates more closely with the functional magnetic resonance imaging (fMRI) BOLD signal [29], which is a measure of blood-oxygen level that exploits the coupling of neural activity and cerebral blood flow [30]. This connection suggests the two signals may encode similar local synaptic activities, which also suggests the insights obtained from each signal individually may be pooled to some extent. Third, because the

LFP mainly conveys aggregated, sub-threshold synaptic input, whereas spikes reflect neural output, the two signals in many cases encode different information [11,31,32]. Importantly, Zanos and collaborators showed that obtaining the LFP with a more sophisticated spike-removal algorithm than low-pass filtering can eliminate artifacts that produce exaggerations in spike-LFP correlations [33]. Fourth, the oscillatory nature of the LFP makes it conducive to analysis in the frequency domain, as well as the time domain. Producing and investigating time-frequency spectrograms (see section 2.4.2) has proven to be a useful technique [34,35], and it facilitates the independent inspection of frequency bands, which have been shown to encode different information in both motor (eg. [36,37]) and sensory (eg. [38,39]) settings. In combination with its previously mentioned long-term robustness these properties make the LFP an appealing signal for clinical prosthetics applications.

1.3.2 Saccades and smooth pursuits

Saccades and smooth pursuits are the two ways that primates can make voluntary eye movements. Saccades are rapid eye movements made between two points without the capacity for correction or alteration during motion. This is because they occur on short time scales (~20 ms) and are not guided by continuous feedback. Rather, they can be corrected with further saccades after the previous ones are complete. They serve to rapidly and optimally position the fovea for best possible vision. Not only is this important to ensure the most sensitive part of the retina is well used, it is also important due to cortical magnification: the phenomenon in which, surface area-wise, disproportionate cortical resources are dedicated to processing foveal input [40]. Similarly, smooth pursuits – or simply, pursuits – allow primates to foveate moving targets with slower, tracking eye movements. Unlike saccades, pursuits necessarily use visual feedback to maintain accuracy over longer periods of time.

At least three areas of the primate brain are responsible for saccade generation: the frontal eye fields (FEF), the supplementary eye fields (SEF), and the parietal eye fields (PEF) [41]. PEF lies within the lateral intra-parietal cortex (LIP), which plays a central role in transforming visual stimulus into eye movement intentions. This is further discussed in 1.3.4. SEF is important for

triggering memory-guided saccades and planning saccade sequences, while FEF is responsible for triggering predictive and visually guided saccades. PEF shares several responsibilities with FEF and is important for reflexive, visually guided, and exploratory saccades. These three cortical areas are critical for saccadic movements, but make up only a small subset of the system governing eye movements; the same is true for smooth pursuits.

Recent work has shown that pursuits are governed by an anatomically parallel system to saccades [42]. It may not be surprising that the systems are closely linked; saccades often precede and intercede pursuits in order to rapidly reduce the error signal between desired and actual eye position. Areas FEF, SEF, and PEF/LIP each perform important functions for proper pursuit movement. FEF lesion studies have demonstrated the area's significance for ongoing, predictive pursuits, which may be required for tracking an oscillating target [43], while SEF stimulation has revealed a primary role in production of anticipatory pursuits [44]. LIP and other intraparietal areas have been studied less in the context of pursuits, but direction-specific tuning – elevated or inhibited neural response corresponding to movement direction – has been observed [45,46]. As with saccades, the system responsible for pursuit generation and maintenance extends far beyond these areas, and some mechanisms are still not well understood. Barnes provides an in-depth review of the current consensus [47].

More pertinent than the mechanistic workings of eye movements is the role they play in providing sensory information to the motor planning and execution areas of the brain. Because primates naturally look where they are reaching and moving, understanding how the brain incorporates visual stimulus and its (objective and relative) spatial location into reach plans is important for building effective neural prosthetic systems.

1.3.3 Cortical pathway for visually guided reaching

The primate visual system is comprised of many regions of the cortical and sub-cortical brain that perform a wide range of functions. Visual input is captured by the eye when photoreceptor cells in the retina are stimulated. The input propagates through the optic nerve and is then

primarily directed to the lateral geniculate nucleus (LGN). The LGN has six distinct layers, which process stimulus according to the retinal-ganglion cell of its of origin [48]. As the stimulus passes through different layers of the LGN, and then into the primary visual cortex (V1), two distinct – although not strictly defined – subdivisions in the visual pathway begin to arise: the ventral and dorsal streams. Goodale and Milner proposed the streams be classified with emphasis on their functional roles, of perception versus action, respectively, rather than according to their differences in input [23]. The action-centric functionality of the dorsal stream makes it most relevant to visually guided reaches.

Each component of the dorsal pathway plays a specialized role for visually guided reaching. After the input signals are processed in area V1, the dorsal stream continues to the posterior parietal cortex (PPC), on to the pre-motor cortex (PMC), and then to the primary motor cortex (M1), where the final motor commands are formulated before transmission through the brain stem to the spinal cord [49]. From the time that the minimally pre-processed visual stimulus enters V1 to the point when the motor command is transmitted down the spine, several intermediate steps must take place. For example, the eyes capture the target and other visual input in retinotopic coordinates, meaning the target's location is defined by the location of its projection onto the retina. However, knowledge of the target's retinotopic position, or even its position relative to where the eyes are looking, is not sufficient to execute an accurate reach. The brain must also be continuously accounting for the position of the head, shoulder, arm, and hand, at minimum. This tracking can occur visually to an extent, but also requires proprioceptive and, sometimes, auditory feedback. The complexity of the task ultimately requires multiple reference frames to encode relative positions of all moving parts under general conditions. As such, the constituents of the dorsal pathway must determine the correct movement vector – the desired net motion of the hand – through a series of coordinate system transforms [50].

The set of computations required to perform these transforms and produce motor commands from visual, auditory, or other sensory input, is called sensorimotor integration. Trotter and Celebrini demonstrated that the process begins as early as V1, which receives retinotopic input from the eyes [51]. Their experiment showed that position of the eyes, or gaze angle, in addition to position of the target on the retina was required to explain the observed response of a large

fraction of V1 neurons. A more recent fMRI study confirmed that early visual areas in humans, like in monkeys, encode stimulus in eye-centered coordinates [52]. Thus, a three-dimensional representation of space, necessary for making sophisticated reaches, begins taking shape in the visual cortex. Momentarily bypassing areas PPC and PMC, which are covered next in 1.3.4 and 1.3.5, a very different picture arises in M1. Gaze location has almost no bearing on neural activity, while position of hands and other dynamic body parts strongly modulate responses in specifically concentrated sub-regions. This has been demonstrated practically in studies such as [53], in which a support vector machine with Gaussian kernel was trained on spike counts from M1 neurons – recorded during reaction time between a cued reach and reach execution – that consistently responded to arm movements. Because M1 output is directly projected to the spine [49], followed by the musculature required for reach execution, the authors were able to accurately decode the subject’s reach intention just before movement onset. Since M1 neurons respond with respect to the position of moving body parts, while visual stimuli, including reach targets, are encoded in an eye-centered reference frame, the conflicting representations must therefore be resolved in PPC and PMC.

1.3.4 Posterior parietal cortex

In 1987, Andersen proposed that the reception of input from visual, auditory, and somatosensory areas, and transmission of output to pre-motor and motor areas could indicate an important role for the posterior parietal cortex in sensorimotor integration [54]. A number of lesion studies have since solidified this argument. Patients with PPC lesions often experience apraxia, which manifests as an inability to plan and execute simple motor tasks when prompted, despite comprehending the request and possessing the physical capability. For example, human patients who suffer from ideomotor apraxia may not be able to demonstrate how to pick up a phone as though it were ringing when asked, yet are able to answer the phone without any problem when it actually rings [55]. Similarly, other subjects with a PPC lesion experience optic ataxia [56]. While their ability to observe and identify a target object, as well as their ability to make voluntary arm movements, remains in tact, hand-eye coordination is severely degraded and results in extreme difficulty when attempting to reach and grab the object. In all such cases,

sensory information is properly processed (the auditory request to pretend the phone is ringing is comprehended, and the target object is visually identified) and motor function is available (the phone can be answered when actually ringing, and reaching motions can be made in general), yet the sensory information cannot be properly transformed into the desired motor plan. Therefore, PPC lesions result in a clear deterioration of sensorimotor integration faculties.

The PPC is composed of sub-regions that lie within and around the intraparietal sulcus, and it occupies Brodmann's areas 5 and 7. Mounting evidence suggests that the different PPC sub-regions each maintain topographic spatial maps of movement intention corresponding to various motor body parts. Sakata and collaborators have demonstrated the specialization of the anterior intraparietal cortex (AIP) for grasping motions by observing strong neural activation patterns associated with objects of certain shapes and size, as well as for certain configurations of the hand [57,58]. As noted in 1.3.2, area LIP encodes information related to saccades and pursuits, and eye position in general. Multiple groups have shown that eye movement intention variables, such as direction and magnitude, can be decoded from LIP spike and LFP signals in both offline [59] and online [60] settings. The medial intraparietal area, which is directly adjacent to LIP, accounts for a significant fraction of the parietal reach region (PRR). PRR, which also includes visual area 7a and the dorsal parieto-occipital area [61], features a high concentration of neurons that are sensitive to planned reach direction relative to gaze position, even in cases when an actual reach is not executed. In all of these sub-regions, the output is related to movement intention; however, integration of sensory information is vital for motor planning in each case.

Sensorimotor integration in PPC also involves more computationally intensive processes than simply mapping a stereotyped neural response to shape or direction, as described previously. Andersen and Mountcastle were the first to find evidence for the existence of cortical gain fields in their 1983 study of area LIP [62]. Gain fields were hypothesized as an encoding scheme capable of describing complex motor plans and movements, often involving coordination of multiple effectors. The underlying theory is that a given brain area will encode a stimulus or intended action relative to a corresponding reference frame, resulting in a baseline neural response. However, the magnitude, or gain, of this neural response is multiplicatively modulated by the input from other neurons that are encoding a secondary variable. In the case of area LIP,

the retinotopic position of a target stimulus, with a fixed central gaze, defines the baseline response. As the subject alters gaze angle – while target position is also altered to ensure its location on the retina stays constant – the directional tuning remains unchanged, but the magnitude of the neural response varies approximately linearly. This was observed for both horizontal and vertical gaze angle changes in [62]. Since then, gain field encoding has also been discovered in area V1 [63], the parieto-occipital sulcus [64], and several other regions of the cortex and sub-cortex, with modulation due to factors like attention [65] and head position [66].

In 2009, Chang and collaborators made a significant breakthrough in visually guided reaching by discovering gain fields in PRR [67]. Their experiment required the macaque subject to simultaneously fixate and touch targets on a screen that were separated by 15° , before completing a peripheral reach without moving his eyes. By varying whether the touch or fixation target was closer to the eventual reach target, the authors determined that both eye and hand gain field neurons exist in PRR and that their activity is negatively correlated. A collection of such neurons results in a combined gain field that modulates neural activity according to the distance between the subject’s hand position and gaze position before movement onset. On a broader level, the existence of PRR gain fields provides a theoretical avenue for performing coordinate transformations from an eye-centered to a hand-centered reference frame. Specifically, the brainstem and somatosensory cortex use efference copies – internally rerouted versions of motor commands – and proprioceptive feedback to track hand and eye position, and provide this information as input to PRR [68]. Since PRR has neurons that can encode hand position in eye-centered coordinates, a vector representing eye-centered hand position can be computed, say \overrightarrow{EH} . Similarly, PRR receives target position in eye-centered coordinates from V1, so it is possible to determine a vector representing eye-centered target position, say \overrightarrow{ET} . Finally, to obtain the reach error-signal, which is the hand-centered target vector, \overrightarrow{HT} , hand position must be vector subtracted from target position in eye-centered coordinates: $\overrightarrow{HT} = \overrightarrow{ET} - \overrightarrow{EH}$. When gaze is fixed on the target, this is the exact computation that PRR gain fields facilitate. Although this is not the only model for coordinate transformations with gain fields (see [67]), its existence demonstrates the importance of gain fields in particular, and the role of PRR and PPC for visually guided reaching in general.

1.3.5 Pre-motor cortex

Like PPC, PMC is a sensorimotor area with sub-regions specialized for a variety of motor tasks. Due to its connectivity with the spine, it may have a direct motor control function, but it is also known to be involved with movement planning. PMC is located in Brodmann's area 6, and is downstream from PPC in the visual pathway, with the latter projecting signals directly to the former [69]. PMC is generally sub-divided according to its ventral and dorsal aspects, PMv and PMd, respectively, and sometimes further into rostral and caudal regions. The rostral region of area PMv is known to be specialized for grasping [70], and neural stimulation studies have also demonstrated its involvement in coordinated movements involving the hands and mouth [71], such as those required before biting into an apple. The caudal PMv region appears to be more sensory oriented, with neurons that are especially sensitive to tactile stimulus and nearby, possibly threatening, objects [72]. Areas FEF and SEF, which also reside in the frontal lobe, both border PMC; however, they are not generally included as a sub-region. Finally, area PMd is part of the dorsal visual pathway and is an important contributor to visually guided reaching.

The location of area PMd in the motor cortex and its position in the dorsal visual pathway are both highly suggestive of its role in reaching. It has been shown to have output connectivity to both the primary motor cortex [73], commonly known as M1, and the spine [49], while receiving input signals from PRR [69]. More concretely, lesion studies have demonstrated decreased reach planning ability when PMd is damaged. For instance, Moll and Kuypers repeatedly observed macaques with PMd lesions reach directly into a solid, transparent obstacle in an attempt to grasp food on the other side [74]. The subjects were aware of the obstacle, but could not formulate a movement plan to reach around it. Micro-stimulation and recording experiments conducted throughout the 1990s and early 2000s revealed strong neural correlations with reach related variables, including reaction time, reach amplitude, and direction [75,76]. Then, in a 2006 study, Pesaran and collaborators discovered evidence of a "relative position code" in PMd that unified several of the previous results [77].

The relative position code means PMd uses a reference frame that encodes the relative positions

of the eyes, hand, and target. This differs from MIP/PRR, where target position is encoded only relative to the eyes. In essence, a relative eye, hand, and target reference frame implies that, regardless of objective spatial position or position relative to the head, shoulders, or other body part, the same configuration of eye, hand and target position with respect to one another will evoke the same neural response. To verify this, the authors held the relative position of two of the variables constant and adjusted the third across a range of values. Of the 111 PMd neurons they studied, 63 were found to encode at least one of the eye-hand, eye-target, and hand-target relative position vectors, and of those 63, roughly 40% encoded two or more, with almost 25% encoding all three. With each of these neurons, the authors verified the encoding could not be explained by the multiplicative effects of gain fields; however, gain field signals from MIP may project relative position input to PMd to help construct the reference frame. While the exact computational details are yet to be proven, the relative position code in PMd, along with eye-centered gain fields in PRR, provides a powerful technique for determining hand-centered reach vectors from stimulus that was originally in retinotopic coordinates.

1.3.6 Motor versus cognitive control of neural prosthetic systems

The importance of areas PPC and PMC to motor prosthetic systems extends beyond the reach mechanics they encode. Rather, both have played an important role in the emerging focus on cognitive neural prosthetics, which use higher level, goal-related control signals.

Early motor prosthetics generally relied on specific trajectories decoded from the motor cortex or other frontal areas. For example, to reach an apple 30 cm to the left of current hand position while a fragile obstacle lies on the most direct path, the subject must devise a multi-step strategy to complete the movement. This would involve continuously updating the reach plan to reflect new circumstances. Rodent and primate studies provided plausibility for this technique [78,79], but several problems became evident. While it is intuitive to use signals that are directly projected to the desired motor effector, the bandwidth required to record and process the activation patterns that produce the muscle trajectory in real-time can be prohibitive [80]. Further, the inevitably imperfect reconstruction of the original signal can lead to broken and

unnatural movements. However, as recording techniques and computing algorithms improve, trajectory decoding from motor areas may become more viable. Recent studies with tetraplegic human patients have already demonstrated that signals recorded from the motor cortex can guide reach and grasp movements with at least seven degrees of freedom, using a robotic [81] or artificially-stimulated natural arm [12].

An alternative to determining complete movement trajectories is to decipher a subject's movement intentions, and then use an intelligent robotic system to map a trajectory and execute the motion. This is the idea behind cognitive neural prosthetics [82]. When the subject aims to reach to the same apple as before, the visual stimulus paired with "intention" should be sufficient to identify the target and desired action. Software designed to formulate a trajectory around problematic obstacles – perhaps in conjunction with additional neural or external data – can then provide the detailed plans required to complete the movement. The defining feature of intention – as opposed to motor – signals are their independence from movement execution. In other words, an intention signal should not rely on the actual occurrence of the planned movement (or, in the absence of a functional motor effector, the projection of movement signals down the spine).

In 2002, Buneo and collaborators were the first of several groups to demonstrate that PRR encodes reach-related intention information [83,84]. In 2004, Musallam and collaborators verified these findings with a primate brain-control study, and showed PMd may also encode intention [15]. The Musallam experiment required the subjects to, first, make physical reaches to a previously cued peripheral target after a 1.2-1.8 s memory period. Using these trials to train the decoder, the macaques then performed brain-control trials, in which no movements were permitted. The decoder was run from 0.2-1.2 s during the memory period; the lower bound was set to prevent any possible influence on the recorded signals from the target cue, and the upper bound ensured the signals were intention-related, rather than related to a suppressed movement. After a few weeks of training, roughly two-thirds of brain-control trials were successfully decoded on an eight-target task using sixteen PMd neurons. A similar success rate was achieved on a six-target task with eight PRR neurons. Additional cognitive variables, such as behavioral state and expected reward, can also be decoded [85]. For reaching tasks, a subject's possible

behavioral states could include resting, cue observation, movement planning, and movement execution. Identifying behavioral states, and especially transitions between states, can convey important temporal information about movement timing [59]. Expected reward – also called expected value – is meant to capture a snapshot of the subject’s frame of mind. In primate experiments, it has been studied by previewing the upcoming (juice) reward that is contingent on successful completion of a trial. Perhaps unsurprisingly, a subject’s reward history – in the case of primate, pigeon, and presumably, human subjects – can be used to predict future behavior [86]. The conceivable applications for each identifiable cognitive variable are wide-ranging, and it is possible that such variables can be decoded from many brain areas. However, the sensorimotor PRR and PMd areas have proven well suited for neural prosthetics.

1.3.7 Decoding algorithms

Thus far, we have identified PRR/MIP and PMd as sensorimotor cortical areas that are of central importance to movement planning and execution (1.3.3-1.3.5). We have introduced the LFP that, as an alternative neural signal to spikes, is relatively easy to record, is robust over the course of years (1.3.1), and importantly, may encode motor and cognitive variables that are essential to the success of prosthetic systems (1.3.6). We now conclude this review with a brief overview of decoding algorithms, which play an integral role in all motor prosthetic systems.

Decoding algorithms translate recorded neural signals to a set of commands that produce desired movements – or more generally, output – from an artificial effector [87]. This output could be reaching conducted by a robotic arm, cursor movements or button presses on a screen, electrical muscle stimulation in a natural body part, or custom control of an assistive device [88]. The algorithms are generally direct applications of one or more statistics or machine learning techniques, and usually fall into one of two categories: regression or classification.

Regression algorithms are used to decode continuous variables from an input signal. This is the case with hand or eye trajectories, for which it is desirable to know position as a function of time to a high degree of precision, in one-, two-, or three-dimensional space. The Kalman and Wiener

filters are commonly used linear techniques for trajectory prediction [87]. The Kalman filter (see [89] for a simple mathematical derivation) is a probabilistic Bayesian inference technique for estimating continuous variables, such as position and velocity. It is an ideal algorithm for real-time applications because it is linear, and thus computationally palatable, and it features the recursive, or Markov, property of making future estimates based only on the present input signals, the most recently estimated state, and the given type of noise. Mulliken and collaborators trained a macaque to use a joystick to control a cursor and select one of eight peripheral targets while maintaining central eye fixation [90]. Using the recorded PPC signals to train a Kalman filter, the subject was then able to produce similar cursor trajectories in brain-control trials without the joystick. Taking a step towards cognitive neural prosthetics, the authors then incorporated goal-based signals into the filter and improved accuracy and timing results to nearly level the attained with the joystick. In a recent offline analysis, Friedman showed that pursuit trajectories could be decoded with a Kalman filter from neuron spike signals in areas MIP and PMd [91]. In contrast, non-linear algorithms, such as artificial neural networks and particle filters, can more accurately model the data by occupying a larger state-space, but can be opaque to interpretation. Further, added computational complexity may limit their clinical viability in the near- to mid-term picture. However, small, non-linear extensions to linear algorithms are beginning to show promising results, as they add flexibility to the models without drastic increases in computational burden (e.g. [92]). As machine learning research continues to advance, regression decoding algorithms are likely to become more effective as well.

When the variable to be decoded is discrete and has a small number of possible outcomes, classification methods become more appropriate. Predicting an intended movement direction, identifying movement type, and classifying behavioral state are all examples of classification tasks. The naïve Bayes classifier (NBC) is a commonly used algorithm for neural classification tasks. Given a set of labeled training examples, the NBC returns the maximum *a posteriori* estimate of the classification variable for an unlabeled test example, which is just the maximum likelihood estimate weighted by prior belief (see 2.4.4 or [93] for a detailed derivation). Using the NBC Scherberger and collaborators, recording from PRR, reported offline, average classification accuracies well above 80% for eight-target, center-out reaches using both spikes and LFPs [31]. In a delayed saccade task, they obtained 40% accuracy using LFPs and over 70%

using spikes. They also used the NBC to discriminate between baseline, movement planning, and execution behavioral states with an accuracy of over 90%. Their strong results in each case demonstrates the NBC's versatility. K-nearest neighbors, which assigns a test example the same label as the plurality of its K nearest neighbors in a labeled training set, and support vector machines, which minimizes an objective function to determine an optimal weighting vector (see 2.4.7), are two other well-known classification algorithms that have achieved good results for neural classification tasks.

While appropriate algorithm selection is critical to successful decoding, even the best algorithms are currently limited by problems like the non-stationarity of neural processes, the apparent randomness and noisiness of neural signals, the large number of variables simultaneously encoded by the brain, and most of all, the minuscule fraction of data that can be recorded from the brain at any given time. Advances in adaptive algorithms, improvements in recording technology, and emerging research in fields like cognitive neural prosthetics, are helping to mitigate these issues, but a great deal of work remains.

1.4 Objectives

MIP and PMd are well-established reach planning areas, and there is also evidence that LFPs from these regions explicitly encode eye movement variables [31]. Because reaches are encoded relative to eye position in MIP and PMd [14,59], simultaneously decoding eye position and reach planning variables could be important for improving motor prosthetic performance. However, the impact of reach planning on LFP oculomotor encoding has not previously been studied. As a first step towards determining the extent of oculomotor encoding under such conditions, we posed two hypotheses:

- i) During reach planning, band-averaged LFP spectral powers from areas MIP and PMd are statistically correlated with saccade and smooth pursuit eye movement directions in at least some frequency ranges. The correlations can thus be exploited to decode

- movement direction on a single-trial basis.
- ii) During reach planning, the same spectral signals in MIP and PMd correlate with eye movement onset time in at least some, but not necessarily the same, frequency ranges. The correlations can thus be exploited to decode time of movement onset on a single-trial basis.

To test the hypotheses, we can consider a simple, discretized model for eye position, in which movements can only be made from a central target to one of four peripheral target locations – up, down, left, or right. To fully characterize eye position as a function of time, it is then sufficient to identify the time at which movement onset occurs, the direction of the movement, and the type of movement – either saccade or pursuit. To control the movement type variable, we can start by treating saccades and pursuits separately and assume each movement is identical to all others of its type.

Inserting this model into a reach planning context enables us to study the impact of reach planning on the signals recorded before, during, and after the eye movement. Consider a reach planning period initiated by a peripheral cue – which can be in either the same or a different direction from the upcoming eye movement – signaling the required end point of a center-out reach. A visual stimulus then instructs the eye movement: for saccades, a peripheral target appears, cuing immediate execution; for pursuits, a central fixation target drifts smoothly outwards, prompting an immediate tracking movement. After eye movement execution, the planning period ends, and the previously cued reach can also be executed.

The experiment that generated the data for this study, which is detailed fully in section 2.3, was conducted in a manner substantially similar to the idealized situation described above. By analyzing LFPs recorded during such a look-reach behavioral task, we can determine the effects of reach planning on movement direction and onset time encoding. To accept the null hypotheses i) and ii) identified above, there must necessarily exist frequency bands in the LFP power spectrum that are statistically correlated with eye movement direction and onset time. Such correlations would constitute *directional tuning* and *temporal onset tuning*, respectively. If no

systematic modulations exist, eye movement direction and onset time cannot be reliably decoded from spectral power. If tuning is established, and assuming an appropriately trained decoder is implemented for each purpose, further observations should be expected:

- i) We might expect that an overall direction decode rate significantly above chance would indicate eye direction is encoded by MIP and PMd LFPs. However, this is insufficient. For example, when a reach is planned in the same direction as eye movement, we cannot be certain that eye direction was decoded, as opposed to intended reach direction. To gain more insight, we can isolate *cis-directional* and *trans-directional* trials, corresponding to trials for which eye and reach direction are the same, and for which eye and reach direction are different, respectively. (The terms “cis” and “trans” are Latin, meaning “on this side” and “on the other side,” respectively.) We can further subdivide trans-directional trials into *opposite* and *perpendicular* classes, again referring to the eye movement direction relative to the reach direction. If MIP and PMd LFPs do encode eye direction independently of reach direction, we should obtain above-chance decode rates for at least two of cis-directional, opposite trans-, and perpendicular trans-directional trials. This would imply that objective eye direction is encoded in the LFPs, not direction relative to an intended reach. Alternatively, if eye direction is not encoded in the LFPs independently of reach direction, we may still obtain an overall above-chance decode rate, but due to only one type of relative eye-reach direction encoding.
- ii) Onset detection is more straightforward because there are no obvious temporal reach planning features to specifically confound eye related signals at onset time. Therefore, if decoded onset times are significantly concentrated near actual onset times, it would be clear evidence that eye-related temporal information is encoded in MIP and PMd LFPs.

In chapter 2 we describe the specific methodology used to test hypotheses i) and ii). In chapter 3, we present results that largely affirm hypotheses i) and ii), which suggests that, to varying extents, eye movement variables are explicitly encoded in macaque MIP and PMd LFPs.

2. Theory and methods

In this chapter, we describe the experimental methods and present the theoretical basis of our analysis. In sections 2.1-2.3, we review animal care and data acquisition procedures, then present the behavioral task performed by the non-human primate subject. In section 2.4, we describe the data analysis techniques that were used to compute spectral power of the local field potentials (LFPs). The naïve Bayes algorithm for directional decoding and the support vector machine algorithm for onset detection are also presented. The results produced by the methods described throughout chapter 2 are reported in chapter 3.

All data analysis performed for this study was completed using custom MATLAB scripts unless otherwise stated (MathWorks, Inc., Natick, MA).

2.1 Animal subjects, care, and surgical procedures

All animal care and surgical procedures were performed by Dr. Sam Musallam, Dr. Greg Stacey, and McGill University Animal Care staff. The data used for this study was collected from electrode arrays implanted in the brain of an awake and behaving, 11.9 kg, male macaque (*Macaca Mullata*). The subject was surgically fitted with an MRI-compatible head post (Rogue Research, Montreal, QC) and trained on the behavioral task (see section 2.3) for nine months before array implantation. The arrays were implanted in the left medial intra-parietal (MIP) and dorsal pre-motor (PMd) areas. Brainsight MRI surgical software (Rogue Research) was used for anatomical localization.

Left hemisphere cortical areas MIP and PMd were implanted with multi-electrode micro-arrays (Microprobe Inc., Bethesda, MD) to obtain contralateral recordings, as the subject was trained to reach with his right hand. The subject had four 16-channel arrays implanted in area MIP and one 32-channel array implanted in area PMd (see Figure 1A). To obtain a cross-section of depths in the intra-parietal sulcus, electrode probes on the MIP array ranged from 1.0-9.0 mm in length. The length of PMd probes ranged from 0.5-1.5 mm.

All surgical procedures were conducted under sterile conditions. Intramuscular Glycopyrrolate (dose: 0.005 mg/kg) was administered to reduce salivation, and then general anesthesia was induced with Ketamine (dose: 10 mg/kg). Anesthesia was maintained with 1-4% isoflurane gas, and a technician remained present to monitor the subject. For ten days post-surgery, analgesics were administered to the subject for pain control.

Training and recording sessions did not resume until more than two weeks after surgery. Throughout recovery and data collection, the subject's weight and growth was monitored daily. The monkey was pair-housed and allowed access to exercise areas, and after each completed data collection session was given fresh fruits. All animal-related experimental procedures were approved by the McGill Animal Care Committee and complied fully with the Canadian Council of Animal Care guidelines [94,95].

2.2 Electrophysiology and data acquisition

All data acquisition was performed by Dr. Greg Stacey and Dr. Sam Musallam. During each recording session, 32 channels from MIP and 16 channels from PMd, for 48 channels total, were recorded simultaneously. A 20x Plexon head-stage initially amplified the raw signals (Plexon Inc., TX), with measurements sampled at 40 kHz. Spikes were initially sorted online with accompanying Plexon software, and sorting, as well as LFP processing (see 2.4.1), was completed offline with custom software. Eye position was tracked with an infrared reflection camera system (ISCAN, Boston, MA), while hand movement was tracked with an acoustic touch screen that was mounted on a monitor (ELO Touch, CA). All training and data collection was conducted in a grounded, copper Faraday cage with LabVIEW real-time software used to coordinate experimental apparatus and recording equipment (LabVIEW RT, National Instruments, QC).

2.3 Behavioral task

The macaque subject was trained to complete a center-out look-reach task. He sat approximately 45 cm from the touch screen, viewing the plane of the screen along the normal direction. Three variants of the task were conducted, with each variant labelled according to the required eye movement: (i) saccade; (ii) pursuit; or (iii) fixation.

In each variant, the subject initiated a trial by visually fixating a central red cross target and touching a central green circle target for 700 ms. Once initiated, a trial was aborted if the subject's gaze or touch moved outside an invisible 2 cm radius of the respective targets. While maintaining the central targets, a peripheral cue was flashed for 600 ms in one of the up, down, left, or right directions, indicating reach direction. After cue offset, a variable-length memory period began, at which point the trial variants diverged (Figure 1B shows all target and cue positions, and Figure 1C provides a schematic of the three trial variants):

- i) For saccade trials, the central fixation target extinguished 600-800 ms after the beginning of the memory period and reappeared 10 cm from the central target in one of the four peripheral locations. The subject was required to make a saccadic eye movement to the new target location while maintaining contact with the central green touch target until the end of memory period.
- ii) For pursuit trials, the central fixation target began moving smoothly in one of the four cardinal directions 700-900 ms after the beginning of memory period, ending 10 cm away at the corresponding peripheral location. The subject was required to track the target with a pursuit eye movement while maintaining contact with the central green touch target until the end of memory period. The duration of each pursuit movement was approximately 1250 ms.
- iii) For fixation trials, the subject was required to maintain gaze on the central fixation target and keep his finger on the central touch target until the end of memory period. Fixation trials were not used for this thesis.

For saccade and pursuit trials, memory period ended 200-700 ms after eye movement completion, at which time the central touch target was extinguished before reappearing at the peripheral location specified by the earlier direction cue. The subject was required to complete a reach to the new peripheral target location, 7 cm from the central target, while maintaining fixation on the visual target. If all steps were completed successfully, the trial ended with the subject receiving a juice reward. He could immediately start the next trial by once again fixating and touching the central targets.

Schedules for the variants were set before recording. For some sessions the variant order was not chosen randomly, so many trials of a single variant could occur successively. However, the subject could never be certain about the variant or movement directions before partaking in the trial. Each session included at least 20 successful trials corresponding to each of the three variants and each of the four reach directions, for a total of at least 240 trials. In sessions M645 and M245 all eye movements were cis-directional – made in the reach direction – while in sessions M246, M456, and M256, both cis-directional and trans-directional eye movements – made to a different direction than the reach – were performed. Accordingly, we defined sessions M645 and M245 as *exclusive* data sets, and M246, M456, M256, as *inclusive* data sets. Both saccade and pursuit trials were used, but treated separately throughout this study. Fixation trials were not used.

2.4 Data analysis

2.4.1 Data pre-processing

Extracting LFP spectral power – our candidate control signal – from the recordings required several processing steps. The micro-electrode arrays recorded potential signals featuring a combination of high frequency activity – including spikes from nearby neuron units – and lower frequency activity, primarily constituting the LFP signal. To isolate the LFP from each of the 32 MIP and 16 PMd channels of each session, we low-pass filtered the raw potential signals using a

first-order Butterworth filter with a 500 Hz cut-off frequency. The signals were then down-sampled to 1000 Hz, such that the resulting LFP had millisecond resolution. Figure 2A shows a single-channel LFP from MIP obtained during a cis-directional, rightward saccade trial.

We aligned the trials so time $t = 0$ ms coincided with eye movement onset for saccade and pursuit trials. Because several task epochs, such as memory period and eye movement execution, had varying durations on a trial-by-trial basis, the timing of cue onsets and reach executions were not aligned across trials. However, due to our primary focus on the relatively short time interval around eye movement onset, such misalignments should have a negligible impact on the results. Eye movement onset times were extracted from the infrared camera eye-tracking data using a custom script and were manually verified to ensure accuracy. Similarly, reach timing and cue onset and offset times were recorded by and obtained from the touch screen and LabVIEW real-time software.

2.4.2 Multi-taper analysis

To obtain a power spectrum from a stochastic, stationary LFP time series, $x(t)$, of length N and temporal resolution Δt , one can directly compute the discrete Fourier transform, $X(f)$, to estimate the spectral content around a frequency f . The power spectral density, $S(f)$, can then be estimated directly from the transform:

$$X(f) := \sum_{n=0}^{N-1} x_n \cdot e^{-2\pi j n f}, \quad f = \frac{l}{N}, l \in \mathbb{Z}, \quad (1)$$

$$S(f) = \frac{\Delta t}{N} |X(f)|^2, \quad -\frac{1}{2\Delta t} < f < \frac{1}{2\Delta t}.$$

However, due to changes in external stimulus and the subject's cognitive and physical state, obtaining a stationary signal from a pertinent brain area over the duration of a trial is unlikely [34,96]. Since we are interested in the temporal dynamics of the LFP, having a stationary signal would also be undesirable. Instead, we treat the underlying probability distributions as dynamic

and estimate the spectral power accordingly. To do this, we assume the time series is stationary on a shorter time scale and compute the power spectrum on data within a sliding window. This technique is broadly known as a short-time Fourier transform, and multi-taper analysis is often used to obtain a time-frequency spectrogram – spectral power as a function of time – for neural data [11,31,34,35].

Multi-taper analysis is popular for neuroscience applications because it provides a bias reduction technique for spectral estimates on a single-trial basis (see [34] for a more thorough coverage). Specifically, the windowed data signal is multiplied by K pair-wise orthogonal tapers before applying the Fourier transform to each one. This results in K statistically independent estimates of the frequency domain signal. The power spectrum can then be estimated from each one individually before averaging to obtain a single estimate, thus minimizing the impact of a noisy LFP. The set of tapers used in multi-taper analysis are generally the first K members of the Slepian, or discrete prolate spheroidal, sequences. The Slepian tapers are the optimal solution for maximizing spectral concentration in the main lobe – the frequency band $[-W, W]$ Hz, where $2W$ is the resolution bandwidth and W must be less than the Nyquist frequency – while minimizing spectral leakage in the side lobes. To maintain the statistical independence of the spectral estimates, a maximum of $K = 2NW\Delta t - 1$ tapers can be used, where N is now the length of the windowed data. In summary, letting $\tilde{x}_m(t)$ be the windowed time signal of length N , corresponding to the m -th window,

$$\tilde{X}_{mk}(f) = \sum_{n=0}^{N-1} h_n^{(k)} \cdot \tilde{x}_{mn} \cdot e^{-2\pi jnf}, \quad f = \frac{l}{N}, l \in \mathbb{Z}, \quad k \in \{1, \dots, K\}, \quad (2)$$

where $\tilde{X}_{mk}(f)$ is the k -th frequency domain estimate of the m -th window of the time series, and $h^{(k)}$ is the k -th Slepian sequence. Then the power spectrum estimate for window m is

$$\tilde{S}_m(f) = \frac{1}{K} \sum_{k=1}^K \frac{\Delta t}{N} |\tilde{X}_{mk}(f)|^2, \quad \frac{-1}{2\Delta t} < f < \frac{1}{2\Delta t}, \quad K < 2NW\Delta t, \quad (3)$$

and any further spectral analysis can occur as in the case of a simple Fourier transform. In order to produce a time-frequency spectrogram, the m windowed power spectrum estimates – which overlap when the sliding window step size is shorter than the windows – can be treated as columns in a matrix, corresponding to times within the trial, and each row then corresponds to a frequency bin.

For this work, we produced multi-taper spectrograms, as described above, using the *cohgramc* command from the Chronux toolbox [97,98]. After conducting a preliminary cross-validation, we selected 300 ms window length, 25 ms step size, and $K = 7$ tapers as parameters to balance the trade-off between noise reduction and obtaining sufficient spectral and temporal resolution. Following the example of similar studies, we computed the logarithmic power, rather than using linear power estimates, and then averaged the spectrogram for each trial across bins to create 13 broader frequency bands: approximately, 0-5 Hz, 5-15 Hz, 15-25 Hz, ..., 95-105 Hz, 105-125 Hz, and 125-150 Hz. Despite some conflicting evidence [99], previous studies have attained good results by assuming band-averaged LFP log-power estimates are independent and normally distributed when drawn from the same relative time across many trials [31,91,100]; statistical techniques – such as ANOVA and naïve Bayes classifiers (see 2.4.3 and 2.4.5) – that rely on an underlying Gaussian process have proven effective, even with small violations of the assumptions. Figure 2B shows an example log-power spectrogram corresponding to the single MIP channel LFP of the cis-directional, rightward saccade trial in panel A. Panel C shows the across-trial average spectrogram for all cis-directional, rightward saccades from session M645. The time axis values refer to the end of the data windows used to estimate spectral power. This standard was maintained throughout the analysis and ensured all power estimates were causal – influenced only by data recorded before or at the time reported.

2.4.3 Analysis of variance

Analysis of variance – commonly known as ANOVA – is a statistical tool used to study the variation of a continuous random response variable given the label of at least one discrete classification variable. It is a powerful and broad technique that we do not require in its full

generality. As such, we narrow our focus to the case of a single classification or grouping variable that can take a finite number of possible realizations. This is called one-way fixed-effects ANOVA [101], although we simply refer to it as ANOVA. One-way refers to the single grouping variable, while fixed-effects refers to that variable's set of discrete and finite outcomes. See [101] or [102] for a more general treatment.

ANOVA extends the Student *t*-test so a classification variable with more than two outcomes can be analyzed. Specifically, it tests the null hypothesis that the population mean of the continuous response variable, s , is identical given any specified class of the grouping variable, y . If the mean of any group is significantly different from the population mean, the null hypothesis is rejected.

ANOVA is based on three important assumptions [101,103]: i) observations are mutually independent; ii) measurements are comprised of the population mean plus a group mean plus random Gaussian error, such that the measurements of each group are normally distributed; and iii) the normal distribution driving the errors has the same zero-mean, σ^2 variance for every value of y , regardless of the fixed-effects properties (i.e. the group mean). While these assumptions are critical to the theoretical underpinnings of ANOVA, there is substantial evidence that small violations do not significantly degrade performance (e.g. [104,105]).

The actual computation in ANOVA begins with the idea that the total sum of squares, TSS, of the difference between each measurement, s_{ij} , and the population mean, \bar{s} – where i indexes the measurement number and j denotes its group – is partitioned between within-group variation, WSS, and between-group variation, BSS. That is $TSS = WSS + BSS$. We can write this formally as

$$\sum_i \sum_j (s_{ij} - \bar{s})^2 = \sum_i \sum_j (s_{ij} - \bar{s}_j)^2 + \sum_j n_j (\bar{s}_j - \bar{s})^2, \quad (4)$$

where \bar{s}_j is the mean value of group j , and n_j is the number of examples from that group. An *F*-statistic can then be computed as the quotient of mean between-group and within-group

variations. The key to ANOVA is that, because of assumption ii) and iii) in particular, this F -statistic is distributed according to an F -distribution with $(k - 1, n - k)$ degrees of freedom (see [106]), where k is the number of classes and n is the total number of examples. A larger value of the statistic corresponds to a higher probability that at least one of the group means is significantly different from the others. Specifically,

$$F = \frac{BSS/k - 1}{WSS/n - k} \sim F_{k-1, n-k}. \quad (5)$$

Finally, a p-value can be computed by inspecting the cumulative F -distribution, CDF_F , such that $p = 1 - CDF_F(F)$. That is, the p-value is the probability of observing an F -statistic greater than or equal to the one observed. Therefore, by comparing p to a pre-selected threshold, α , ANOVA rejects the null hypothesis if $p < \alpha$. Common threshold levels are $\alpha = 0.05$ or $\alpha = 0.01$.

2.4.4 ANOVA for direction classification

We followed a similar ANOVA procedure to Hwang and Andersen [100], with band-averaged LFP log-power as the response variable, and eye movement direction (left, right, up, and down) as the grouping variable.

We studied four intervals near the time of eye movement onset – T1, T2, T3, and T4, corresponding to reach-memory, pre-onset, peri-onset, and post-onset periods, respectively (see Table 1 for full description) – and repeated the procedure separately at each time for all frequency bands in all channels. Figure 2D shows a visual representation of the relative T1-T4 period locations. These intervals were chosen to help dissociate the effects of reach planning from eye movement direction encoding. Since T1 occurred before the eye movement was cued, any spectral power modulations that varied systematically with eye movement direction – which we call directional tuning – would necessarily be due to correlations between intended reach direction and eye movement direction. T2 was centered at after eye movement was cued, and T3 was centered at eye movement onset. Therefore, directional tuning detected by ANOVA could

Table 1: Description of time periods studied for eye movement direction classification.

| Period label | Period name | Time rel. eye movement onset | Description of time period |
|---------------------|--------------------|-------------------------------------|----------------------------------------------------------------------------------------------|
| T1 | Reach-memory | (-650, -350] ms | Occurred during memory period; finished before eye movement was cued |
| T2 | Pre-onset | (-300, 0] ms | Centered in period after eye movement was cued; last data window prior to eye movement onset |
| T3 | Peri-onset | (-150, 150] ms | Centered at eye movement onset; captured end of movement planning and beginning of execution |
| T4 | Post-onset | (25, 325] ms | Began post-onset, near time of saccade completion; pursuit execution continued throughout |

be due to the change in visual stimulus, especially for T2, movement planning and onset, especially for T3, along with the same correlations as T1. In addition to the eye-reach direction correlations, tuning detected during T4, which occurred after movement onset, could be related to the new eye position – objectively or relative to hand position [31,59] – and for pursuits, could be related to the ongoing eye movement planning and execution.

For each period, we concluded that spectral power signal was directionally tuned in a given frequency band of a channel if ANOVA rejected the null hypothesis, that the mean spectral power corresponding to each eye movement direction is identical, with 95% confidence ($p < 0.05$). If the null hypothesis was not rejected, we concluded the group means were identical and that predictive directional information could not be obtained from the power estimate in that band.

For implementation, we used the MATLAB *anova1* function in combination with leave-one-out cross validation [103]. For a given test trial, all trials from the session, except the test trial, were used as ANOVA input. The process was repeated until all trials were left out as the test trial. Tuning information obtained with a given left out trial could then be used for predictive classification without biasing the results, as described in 2.4.5.

2.4.5 Naïve Bayes classifier

We used a naïve Bayes classifier (NBC) to predict saccade and pursuit movement direction with data recorded during T1, T2, T3, and T4. An NBC is trained on a set of n examples – feature vectors of attributes, (x_1, x_2, \dots, x_m) , corresponding to a given grouping label, $d \in D$, where D is a discrete and finite set. The attributes, s_i , can be continuous- or discrete-valued, and are treated as random variables. Given a test vector, (s_1, s_2, \dots, s_m) , the NBC returns the maximum *a posteriori* (MAP) grouping label, \hat{d}_{MAP} , under some simplifying assumptions. Beginning with the definition and then directly applying Bayes rule

$$\begin{aligned}\hat{d}_{\text{MAP}} &= \operatorname{argmax}_{d \in D} P(d|s_1, s_2, \dots, s_m) \\ &= \operatorname{argmax}_{d \in D} \frac{P(s_1, s_2, \dots, s_m|d)P(d)}{P(s_1, s_2, \dots, s_m)} \\ &= \operatorname{argmax}_{d \in D} P(s_1, s_2, \dots, s_m|d)P(d),\end{aligned}\tag{6}$$

where the final equality holds because the denominator is independent of class label.

$P(s_1, s_2, \dots, s_m|d)$ is the likelihood of the observed attributes given the class, and $P(d)$ is the prior probability distribution for class d . Assuming $|D|$ is relatively small, the priors for each $d \in D$ can be estimated from how frequently they appear in a moderately sized training set; alternatively, the user can demand uniform or other problem-specific priors. However, for even a moderate value of m , obtaining accurate likelihood estimates by counting training set appearances, over the range of each s_i and for each element of D , would require a prohibitive number of training examples.

To circumvent this issue, the NBC makes a strong assumption that each s_i is conditionally independent of s_j for all $i \neq j$ given the class label [93]. This means the likelihood can be written as a product of marginal distributions, which greatly reduces the dimensionality of the required distribution estimation:

$$\hat{d}_{\text{MAP}} = \underset{d \in D}{\operatorname{argmax}} P(d) \prod_i P(s_i | d). \quad (7)$$

At this point, a number of approaches can be taken to estimate the $m|D|$ conditional probability distributions of the individual attributes, depending on the variable types. If the attributes are primarily discrete variables with a small number of possible outcomes, sufficiently accurate estimates could be determined by directly counting relevant frequencies in the training set.

Conversely, if the underlying distributions that govern the attributes are known, the training set can be used to compute corresponding sufficient statistics.

For this study, the attributes were band-averaged log-power estimates corresponding to the directionally tuned frequency bands of each channel – as determined by the ANOVA procedure described in 2.4.4. Once all tuned bands were identified for each channel ($p < 0.05$), we selected the 12 channels (out of 32 for MIP and out of 16 for PMd) with the highest number of tuned bands to use for classification. This standard enabled us to systematically limit the training set size for computational efficiency, while avoiding the most uninformative channels. Further, we reasoned that a channel with more tuned bands would likely have a smaller fraction of spuriously bands, mistakenly identified as tuned due to outliers or coincidental correlations in the training set. Conversely, this logic implies that fair comparisons between areas MIP and PMd cannot be made; if we assume the amount of MIP and PMd channel information were drawn from the same distribution – meaning the expected information of a single MIP and a single PMd channel would be the same – and assume channels with more tuned bands are more informative, then the MIP channels we selected would be drawn from only the top half of the distribution, while the PMd channels would be drawn from the top three quarters.

The grouping labels for the feature vectors were eye movement directions, such that $D = \{up, down, left, right\}$. Since we considered 13 frequency bands and used 12 channels for each test trial classification, m could take a maximum value of $13 \times 12 = 156$. Due to the potentially large number $m|D|$, and because the log-power estimates were continuous-valued, it was not feasible to directly estimate the likelihoods in (7) from the training set.

Instead, we assumed that each estimate was drawn from a univariate normal distribution, which is the same assumption required by ANOVA. To characterize the distributions, it was therefore sufficient to compute the sample mean, $\hat{\mu}_{id}$, and variance, $\widehat{\sigma^2}_{id}$, for the i -th channel-band, $i \in \{1, \dots, m\}$, and the d -th direction label. Then, given a test attribute vector, (s_1, s_2, \dots, s_m) , corresponding to an unknown eye movement direction, the NBC MAP label was

$$\hat{d}_{\text{MAP}} = \underset{d \in D}{\operatorname{argmax}} P(d) \prod_i (2\pi\widehat{\sigma^2}_{id})^{-\frac{1}{2}} \exp\left(-\frac{(s_i - \hat{\mu}_{id})^2}{2\widehat{\sigma^2}_{id}}\right). \quad (8)$$

For implementation, we used the MATLAB Naïve Bayes class [107]. Treating 3-tuple combinations of saccades and pursuits, MIP and PMd, and cis and trans trials separately, we randomly selected the greater of 100 or three quarters of all relevant trials as the NBC training set. Using the directionally tuned channels ($p < 0.05$; ANOVA) for the corresponding test trial, we separately obtained eye movement direction predictions at each of the four intervals. With each trial in the session acting as the test trial, we repeated the NBC classification 1000 times, drawing a new training set, with replacement, after each iteration. We used the case resampling basic bootstrap method to compute confidence intervals [108].

2.4.6 ANOVA for onset detection

We now review methods for eye movement onset detection. To our knowledge, no previous studies have decoded movement onset time from cortical LFPs. Since there are accordingly few standardized procedures, we proposed and implemented a methodology that mirrors the direction classification techniques described in 2.4.4 and 2.4.5. To determine which frequency bands were modulated by an imminent eye movement, we again used one-way fixed-effects ANOVA. The mathematical basis for the technique is exactly as described in 2.4.3, but adjustments were required for application.

For direction classification, all times in each trial were described by a single grouping label; for onset detection, it was necessary to differentiate times near eye movement onset from all other

times. To do this, we considered a 1 second interval in each trial, from 900 ms before saccade or pursuit onset, to 100 ms after onset. Next, we defined a binary grouping variable y , such that $y = -1$ for any window of data that ended in the $[-900, 0)$ ms *pre-onset* period; this constituted the null hypothesis that no movement onset had occurred. Alternatively, rejection of the null hypothesis, $y = 1$, corresponded to any window of data that ended in the $[0, 100]$ ms *onset* period. Due to data alignment and 25 ms sliding window step size, the pre-onset period corresponded to 36 negatively labeled windows, and the onset period to 5 positively labeled windows, per trial. Table 2A summarizes the period and label descriptions, and Figure 2E provides a visual representation of the pre-onset and onset periods. Note that the 300 ms window length means all windows in the onset period were centered 50 ms or more before movement onset. In general, using later windows for detection could improve results, but the increased lag between movement onset and time of detection would reduce the detector's utility.

We used ANOVA to determine which frequency bands demonstrated consistent spectral power modulation in the onset period relative to the pre-onset period. Input was, therefore, comprised of appropriately labeled log-power estimates from the pre-onset and onset periods of training trials. To limit the impact of non-stationarity within the pre-onset and onset periods, we further constrained the input by only using estimates from 50 ms subintervals. In particular, we took the average of log-power estimates from the three data windows ending in the $[-150, -100]$ ms subinterval and from the three windows ending in the $[50, 100]$ ms subinterval. For each trial, the former average value was the single negatively labeled input and the latter average value was the single positively labeled input. By using the averaged value of three estimates from each interval, we obtained some protection against noise while simultaneously limiting the effect of the log-power dynamics over the course of a full second. The relative subinterval locations ensured there was enough time for true modulations to manifest. The subintervals were also close enough to maintain confidence that observed changes resulted from movement planning and execution, not a confounding variable. Finally, we reasoned that, due to task related differences, log-power estimates from early in the pre-onset period should be relatively dissimilar to onset period

Table 2: A) Description of time intervals studied for eye movement onset detection.

| Period name | Time rel. eye movement onset | Classification label | Period description |
|--------------------|-------------------------------------|-----------------------------|--------------------------------------------------------------------------|
| Pre-onset | $[-900, 0)$ ms | $y = -1$ | Reach direction cue offset, memory period, and eye movement cue/planning |
| Onset | $[0, 100]$ ms | $y = 1$ | Saccade onset and completion; pursuit onset and early stage of movement |

B) Description of confusion matrix elements for eye movement onset detection (Note: The logical \equiv operator returns 1 if operands are equal, 0 otherwise).

| Element label | Counts per trial | Notes |
|----------------------|--------------------------------------------------------------|----------------------------------------------------------------------------------|
| TP | $\max\{ y(t) \equiv 1 \mid t \in [0, 100] \text{ ms} \}$ | One TP occurs iff at least one positive detection during onset period, else zero |
| FN | $1 - \max\{ y(t) \equiv 1 \mid t \in [0, 100] \text{ ms} \}$ | One FN occurs iff no positive detection made during onset period, else zero |
| FP | $\sum\{ y(t) \equiv 1 \mid t \in [-900, 0) \text{ ms} \}$ | One FP for every positive detection during pre-onset period |
| TN | $\sum\{ y(t) \equiv -1 \mid t \in [-900, 0) \text{ ms} \}$ | One TN for every negative classification during pre-onset period |

estimates. For our overarching goal of onset detection, it was therefore more important to compare the late pre-onset period – rather than the entire $[-900, 0)$ ms interval – to the onset period.

Through this ANOVA framework, coupled with the same leave-one-out procedure described at the end of 2.4.4, we obtained temporal tuning information for the SVM eye movement detection algorithm described in 2.4.7. Specifically, we determined the significantly onset-tuned frequency bands, with $p < \alpha$, for each channel. The threshold, α , was selected with a parameter optimization grid search, as detailed in 2.4.8.

2.4.7 Support vector machine

To detect saccade and pursuit onset, we used a support vector machine to perform binary classification. We maintained the data-window labels given in Table 2A; the SVM objective was, therefore, to classify data from the [-900 ms, 0 ms) pre-onset period of the test trial as $y = -1$ and data from the [0 ms, 100 ms] onset period as $y = 1$.

In general, SVM classification works by optimizing a vector, \mathbf{w} , using a set of binary-labelled training examples. The \mathbf{w} vector defines a hyperplane that aims to separate the two classes in an optimal way. When the two classes are separable – such that there exists a hyperplane which keeps all negative, $y = -1$, and positive, $y = 1$, examples on opposite sides – the closest example from each class to the hyperplane defines a margin, M . The optimal way in which the SVM separates the training examples is by maximizing M [109]. Thus, the SVM optimization task is

$$\max_{\mathbf{w}}(M) \leq \gamma_i = y_i \left(\frac{\mathbf{w}}{\|\mathbf{w}\|} \cdot \mathbf{x}_i \right) \quad \forall i, \quad (9)$$

where \mathbf{x}_i is a training data vector, y_i is the corresponding label, and γ_i is the distance of the i -th training example from the hyperplane boundary. Each \mathbf{x}_i is padded with a leading one such that the first term of the inner product is a bias offset. Note that if \mathbf{w} is an optimal solution, so too is $k\mathbf{w}$ for any $k > 0$. This means we can further constrain the problem such that $\|\mathbf{w}\| M = 1$, and we can thus reformulate the problem in terms of minimizing $\|\mathbf{w}\|$, or equivalently, $\|\mathbf{w}\|^2$.

In the case of data that cannot be linearly separated by a hyperplane, Cortes and Vapnik proposed a “soft margin” adjustment [110]. With a soft margin, training examples that are misclassified or lie within the margin are allowed, but get penalized. The SVM framework also supports more general transformations of the data in terms of feature vectors, $\phi(\mathbf{x}_i)$. The problem can thus be restated as

$$\min_{w, \xi} \left\{ \frac{1}{2} \|w\|^2 + C \sum_i \xi_i \right\}, \quad (10)$$

subject to the constraints

$$y_i(w \cdot \phi(x_i)) \geq 1 - \xi_i, \quad \xi_i \geq 0, \quad \forall i,$$

where C is a constant parameter that moderates the penalty for soft errors, and ξ_i is the soft error, such that $0 < \xi_i < 1$ if the data point falls inside the margin, $\xi_i \geq 1$ if the point is misclassified, and $\xi_i = 0$ otherwise. C can also be viewed as an overfitting control parameter – by heavily penalizing misclassifications, the optimization focuses on fitting all training examples; by reducing the penalty, a boundary that is less specific to the given training examples can be obtained, and may generalize better to unseen cases. The examples that are either misclassified or that define the classification boundary are collectively called support vectors.

The formulation presented in (10) is called the primal form and is relatively intuitive. However, it can be computationally expensive depending on factors like feature vector complexity and magnitude of the misclassification penalty. This can be partially mitigated by instead solving the dual problem. The dual is achieved by rewriting the primal form as a generalized Lagrangian and imposing the Karush-Kuhn-Tucker (KKT) conditions [111]. The KKT conditions extend the Lagrange multiplier technique to support inequality constraints. Next, w is written in terms of a linear combination of parameters, α_i – which are introduced by the Lagrangian – the feature vectors, $\phi(x_i)$, and the class labels, y_i . Finally, the “kernel trick,” first proposed by Aizerman and collaborators in [112], is employed by replacing all inner product computations with a kernel function. A kernel function provides an alternate expression of inner products in some feature space, $K(x, z) = \phi(x) \cdot \phi(z)$, and the computations can often be done in a lower complexity class.

By applying the kernel trick to SVMs, several classes of decision boundaries can be conveniently investigated. Common kernel choices include linear, polynomial, and radial basis functions (RBF) [109].

After a preliminary inspection of the data and cross-validation over kernel functions, we chose to use the RBF, or Gaussian, kernel for this study:

$$K(\mathbf{x}, \mathbf{z}) = \exp\left(-\frac{\|\mathbf{x} - \mathbf{z}\|^2}{2\sigma^2}\right). \quad (11)$$

We implemented the SVM with RBF kernel using the MATLAB *fitcsvm* function [113]. The function uses training set subsampling to optimize the width parameter σ , but selection of the soft margin parameter, C , and prior class probabilities were still required. Choosing a prior different from 0.5 for each class is equivalent to biasing the classification boundary; due to our problem construction with approximately 90% of data coming from the pre-onset period, we chose 0.9 and 0.1 as prior probabilities for the negative and positive classes, respectively. To select the optimal value of C , along with the ANOVA threshold, α , we used the grid search described in 2.4.8. Once optimal parameters were selected, the temporally tuned frequency bands from each trial were identified. Like in 2.4.5, we used the 12 channels with the most tuned bands for the simulation. Using these 12 bands, one log-power feature vector was constructed for each time in the pre-onset and onset periods. The vector elements corresponded to the tuned frequency bands across all 12 channels. Therefore, the test trial and each training trial produced 36 feature vectors from the negative class and 5 feature vectors from the positive class. We used simple leave-one-out cross-validation on trials from the testing set – defined in 2.4.8 – for the SVM onset detection simulations. Confidence intervals were computed with the Clopper-Pearson method.

2.4.8 Parameter optimization

To select the soft margin constant, C , and ANOVA threshold, α , we required a way to determine which parameter pair corresponded to the optimal SVM classifier. Given the nature of the detection task, we first defined the confusion matrix elements on a single trial level. We counted one true positive (TP) for a test trial if one or more positive classifications (true detections) was

made during the onset period, with no penalty for negative classifications (missed detections). We counted one false negative (FN) if there were only missed detections during the onset period. During the pre-onset period, every positive classification was counted as a false positive (FP) and every negative classification was counted as a true negative (TN). These definitions are summarized in Table 2B.

Because we should ideally expect many TNs and a maximum of one TP over a single trial, a simple metric like accuracy is insufficient. For example, naively making a negative classification at every time step would result in only one misclassification, and thus a high accuracy. However, this technique provides no insight into the dynamics of the problem. Instead, we computed the Matthews correlation coefficient (MCC) using the cumulative confusion matrix across all test trials:

$$MCC = \frac{TP \times TN - FP \times FN}{\sqrt{(TP + FP)(TP + FN)(TN + FP)(TN + FN)}}. \quad (12)$$

It therefore takes a value in the real interval $[-1, 1]$, where $MCC = 1$ means there were no FPs and no FNs , $MCC = 0$ suggests random guessing or repeatedly selecting a single class with probability one, and $MCC = -1$ corresponds to observing only FPs and FNs . Note that in the case of any factor in the denominator being zero, MCC is defined to be zero. An in-depth evaluation of its efficacy is performed in [114].

As a scalar statistic, the MCC provided a natural order on classifier effectiveness for different outcomes due to different parameter values. We used the MCC as an objective function to maximize during a grid search over plausible values of C and α . For each dataset, we used the greater of 40 or the first half of relevant trials as the optimization set for the grid search. The remaining trials from the dataset were set aside as a testing set. Within the optimization set, we applied leave-one-out cross validation, such that the 41 times in the pre-onset and onset periods of each trial were all classified. The cumulative TP , TN , FP , and FN counts for each pair of parameters was then used for computing the MCC according to (12), and the values that

maximized the statistic were used for simulating the testing set trials. The results reported in subsection 3.2.2 are based only on test trials from the testing set.

3. Results

In chapter 3, we report the results obtained from implementation of the methods described in chapter 2. Section 3.1 is related to eye movement direction decoding, with 3.1.1 focused on directional tuning in the frequency bands and 3.1.2 focused on movement direction decoding using the naïve Bayes classifier (NBC). Section 3.2 is related to detecting eye movement onset time, with frequency band temporal tuning results reported in 3.2.1 and support vector machine (SVM) onset decoding reported in 3.2.2.

3.1 Decoding eye movement direction

Recall that for both saccades and pursuits, we defined two types of trials: cis-directional trials, in which eye movement was made to the same direction as the planned reach, and trans-directional trials, in which eye movement was made to one of the three other directions. Accordingly, we differentiated *exclusive* datasets M645 and M245, which contained only cis-directional trials, from *inclusive* datasets M246, M456, and M256, which contained both cis- and trans-directional trials. These distinctions, which are referenced throughout 3.1.1 and 3.1.2, enabled us to isolate the effects of reach planning and eye movement direction encoding on the local field potential (LFP) spectral power, as described in 2.4.4 and 2.4.5.

3.1.1 Directional tuning for eye movements in areas MIP and PMd

We first identified the frequency bands in each channel that exhibited direction-specific responses, or tuning, for saccades and pursuits. Tuning was determined by using a one-way fixed-effects ANOVA (see 2.4.3-2.4.4) to test for equality of mean spectral power across directions. A channel was considered directionally tuned in a frequency band if ANOVA yielded a p-value $p < 0.05$. Figure 3 illustrates two examples of significantly tuned bands. The left panels of Figs 3A and 3B show log-power estimates from the 105-125 Hz band of channel 1 and the 45-55 Hz band of channel 17, respectively, during the peri-onset period (T3) of saccade trials

in session M645. Each data-point corresponds to a single trial, with the colored markers indicating saccade direction, as labeled. The right panels provide tuning curves for each band, in the form of the mean log-powers for each direction, plus or minus standard deviation. According to ANOVA, the 105-125 Hz band of channel 1 was the most statistically significantly tuned band across all channels in the session, with $p = 2.8 \times 10^{-7}$. Meanwhile, the 45-55 Hz band of channel 17 narrowly achieved the threshold to be considered significantly tuned, with $p = 0.040$. In both bands, there were many overlapping data-points between all saccade directions. This indicates the general difficulty of decoding eye movement direction and drawing strong conclusions from tuning results.

With this context in mind, we examined the significantly tuned frequency bands. Figure 4 shows histograms of significantly tuned channels, binned by frequency band, from the pooled set of 64 MIP and 32 PMd channels in the exclusive datasets. The columns, from left to right, correspond to the reach-memory period (T1), pre-onset period (T2), peri-onset period (T3), and post-onset period (T4); the rows, from top to bottom, correspond to saccades with MIP data, saccades with PMd data, pursuits with MIP data, and pursuits with PMd data. Because there were only cis trials in this data, a fixed relation existed between eye movement and planned reach direction, and since T1 occurred before eye movement was prompted, we suggest that tuned channels during T1 should be attributed to reach planning.

Relative to T1, there was generally a higher fraction of tuned channels in bands above 15 Hz during periods T2-T4. As such, the gained channels may have been derived from eye movement planning and execution. The largest increases tended to occur in the 25-75 Hz range in all four cases (rows of Fig 4). For MIP and PMd saccades, these increases appeared in T2 and T3, while for pursuits, they did not manifest as strongly until T3. The discrete and obvious change in fixation target position for saccades, as opposed to the initially small, smooth, and thus harder to detect, change in target position for pursuits, may have caused this difference. However, we cannot be certain from these results that eye movement direction is encoded in MIP or PMd at all. Rather, changes in the distributions could have resulted from ongoing reach planning.

Figure 5 presents similar histograms using data from the inclusive data sets, and better allows us to dissociate eye movement direction from planned reach direction. In all panels, the lighter colored bars correspond to cis trials, and the darker colored bars to trans trials. We do not include trans results for T1 because of the uncertain relation between eye movement and reach directions; since eye movements and reaches were made to different directions in trans trials, any detected tuning would necessarily have been spurious. For saccades in periods T2 and T3, the fractions of tuned channels for cis and trans trials were very similar. After saccade execution, in T4, the trans fractions remained largely unchanged. Meanwhile, the cis fractions grew larger than the trans fractions in all MIP and PMd bands, and the fractions generally increased relative to the T1-T3 cis distributions as well. While the existence of tuned channels for trans saccades suggests LFP spectral power in MIP and PMd does encode the eye movement direction – since the reach to a different direction was unlikely to falsely imply tuning – it remains unclear whether the tuned channels for cis trials were actually caused by the saccades.

For pursuits, the MIP and PMd cis distributions presented in Figure 5 qualitatively matched the corresponding distributions shown in Figure 4, across all time periods. However, a stark contrast appeared between cis and trans pursuits in the 0-35 Hz frequency range of periods T2-T4 (Fig 5, cols 2-4, rows 3-4). In T2, 27.1% of MIP channels were tuned in both the 0-5 Hz and 5-15 Hz bands, while 37.5% and 31.3% of channels were tuned in the same PMd bands. For cis trials, just 1.0% and 5.2% of MIP channels, and 0.0%, and 5.2% of PMd channels were tuned in the 0-5 Hz and 5-15 Hz bands. Notably, the opposite case arose for the 15-25 Hz and 25-35 Hz bands: 2.1% of MIP channels were tuned in each band for trans trials, as opposed to 15.6% and 24.0% for cis trials. In PMd, 0.0% and 18.8% were tuned for trans compared to 43.8% and 35.4% for cis (all percentages relative to the total of 96 MIP and 48 PMd channels used across the pooled inclusive data sets). The same phenomenon persisted through periods T3 and T4 as well. Overall, this 0-15 Hz tuning strongly suggests the existence of a role for MIP and PMd spectral power in determining, or at least having knowledge of, pursuit trajectory. The non-zero fraction of significantly tuned bands, across almost all 0-150 Hz frequencies, for trans saccades and pursuits provides additional evidence.

3.1.2 Predicting movement direction with naïve Bayes classifier

To more concretely verify that directional information is encoded in MIP and PMd LFPs, we used the log-power estimates from significantly tuned bands to decode eye movement direction. For each combination of trial type (cis or trans), movement type (saccade or pursuit), and cortical area (MIP or PMd) we trained a separate NBC, as described in 2.4.5. Figures 6 and 7 show the fraction of correctly decoded saccade and pursuit directions, respectively. For each figure, the left column corresponds to MIP data, the right column corresponds to PMd data, and the dashed, horizontal line marks the chance decode rate of 25%.

Panels A of Figs 6 and 7 show the pooled cis-directional decoding results from the exclusive datasets at times T1-T4. For MIP and PMd saccades, as well as MIP pursuits, the decode rate in the reach-memory period, T1, was not significantly different from the decode rates in either T2 or T3 at the 95% confidence level. For PMd pursuits, the T1 decode rate was actually significantly higher than the T2-T4 decode rates. A literal interpretation then suggests – for cis-directional pursuits from exclusive datasets – rather than decoding movement direction immediately prior to or during execution, one should decode planned reach direction before the cue and use the same answer. The highest decode rates for MIP and PMd saccades were achieved during T4, but recall T4 corresponded to the (25, 325] ms interval relative to movement onset. As such, it did not begin until near or after the end of saccade execution, which could suggest we were primarily decoding planned reach direction in this interval. Overall, because the exclusive dataset saccade and pursuit decode rates for periods T2-T4 were significantly above chance, it is possible that LFP spectral power encodes eye movement direction; however, the saccade classification rates at T1 and T4, and the pursuit classification rates at T1, suggest that concurrent reach planning had a primary impact on the results. This is the same conclusion we obtained from the ANOVA results shown in Fig 4.

Panels B and C of Figs 6 and 7 show pooled direction-decoding results for the inclusive data sets. To obtain the values shown in panels B, we first trained the NBC using only cis trials. We then separately decoded cis test trials – corresponding to the lighter colored bars – and trans test trials – corresponding to the darker colored bars. Similarly for panels C, we trained the NBC

using only trans trials, then separately decoded cis test trials (lighter bars) and trans test trials (darker bars). Also note that we do not include decode rates for T1 with the trans-trained NBC because we did not control the composition of opposite- and perpendicular-trans trials – which refer to the relative eye movement and reach directions – in the training sets. If a large fraction of the training set was opposite-trans trials, for example, the NBC could yield significant, but spurious, results by consistently decoding reaches to a given direction as eye movements to the opposite direction.

In Fig 6B, we observe that cis-trained NBC decode rates were significantly above chance for MIP cis saccades in T3 and T4, and significantly above chance for PMd cis saccades in T1-T4 (95% confidence level). Conversely, trans saccade decode rates were significantly below chance in all cases except for MIP at T2, where the upper confidence interval bound was exactly at chance: 25.0%. Fig 7B shows all cis-trained NBC decode rates were significantly above chance for MIP and PMd cis pursuits, while the upper confidence interval bound exceeded chance for MIP trans pursuits in T3 and T4 only. Similarly, Figs 6C and 7C show that the trans-trained NBC decoded trans saccades and pursuits above chance at the 95% confidence level for MIP and PMd during all times T2-T4. Meanwhile, cis trials were never classified significantly above chance, and were significantly below chance for PMd pursuits during T2.

If eye movement direction were encoded completely independently of planned reach direction – such that an eye movement direction-specific distribution of spectral power could be consistently observed from tuned channels, regardless of reach direction – we would expect the decode rates for both cis and trans trials to be significantly above chance for any sufficiently large training set. Evidently this was not the outcome, as the type of trial used for training was also decoded at a significantly higher rate at all times T2-T4 (panels B and C of Figs 6 and 7). To account for the possibility that intended reach direction had a multiplicative, gain field-type, effect on the log-power response, we tried adding a normalization step to the decoding procedure, such that only relative log-power in the tuned bands was used for decoding. However, all results remained qualitatively similar (plots not shown).

Because cis and trans trials were never simultaneously decoded significantly above chance, we still could not be certain that eye movement direction is encoded in LFP spectral power during reach planning. In particular, the above-chance decode rates for cis trials in Figs 6B and 7B could have been driven by reach direction encoding. Similarly, the above-chance trans decode rates in Figs 6C and 7C could have been driven by reach direction encoding that the NBC conflated with one relative eye movement direction. However, this would require either opposite- or perpendicular-trans trials to be decoded at an above-chance rate, but not both.

Following this logic, we explicitly categorized the trans-directional trials as either opposite or perpendicular, referring to the relative eye movement and reach directions. Using the same decode results as panels C of Figs 6 and 7, Figure 8 shows trans trial classification rates with the additional categorization. Panels A-D show results for MIP saccades, PMd saccades, MIP pursuits, and PMd pursuits, respectively, with the light colored bars corresponding to opposite-trans trials and the dark colored bars corresponding to perpendicular-trans trials in each panel. Both opposite- and perpendicular-trans eye movements were decoded above chance in all cases during all times T2-T4. For opposite-trans trials, 7/12 (58.3%) cases – across brain area, movement type and time period – were decoded significantly above chance at the 95% confidence level, and for perpendicular-trans trials, 9/12 (75.0%) cases were decoded significantly above chance. The simultaneous above-chance classification rates for opposite- and perpendicular-trans trials show that objective eye movement direction was, indeed, decoded, and not eye movement direction relative to the planned reach. Although work remains to successfully decode cis and trans trials with the same classifier, we have presented strong evidence that MIP and PMd LFP spectral power does independently encode eye movement direction during reach planning.

3.2 Detecting eye movement onset

For eye movement onset detection, we no longer maintained the distinction between cis- and trans-directional trials. We also did not differentiate between movement directions. Our goal was, first, to determine which frequency bands in MIP and PMd were modulated by saccade and

pursuit movement onset, and second, to determine how effectively an SVM classifier could exploit these changes across time in LFP spectral power to identify movement onset at the temporal resolution of a 100 ms onset period. The results for the first task are reported in 3.2.1, and results for the second task are reported in 3.2.2.

3.2.1 Temporal tuning for eye movements in areas MIP and PMd

Following the ANOVA procedure outlined in 2.4.6, we determined which of the 13 frequency bands were significantly temporally tuned to movement onset, such that $p < \alpha$. However, the value of α that was used for the onset detection task, reported next in 3.2.2, was optimized with a grid search. For separate study, we used a value of $\alpha = 0.001$ to generate the plots in Figure 9. Fig 9 displays normalized histograms of tuned channels, binned by frequency band, for saccade and pursuit trials classified with MIP and PMd data. Since the heuristic selection of α was somewhat arbitrary, the relative proportions of tuned channels between bands are of greater interest than the absolute fractions. In all four cases, the highest fraction of tuned channels was in the bands between 15-75 Hz. The mode was the 15-25 Hz band for MIP and PMd saccades, 25-35 Hz for PMd pursuits, and 35-45 Hz for MIP pursuits. Very little tuning was present above 85 Hz for pursuits, with the fraction of tuned MIP channels falling below 20% of the mode fraction for all such bands. For saccades, roughly 30-50% of the mode fraction remained tuned in all bands from 85-150 Hz. It may be unsurprising that higher frequency bands were more strongly modulated near saccade onset, relative to pursuits, since saccades are more rapid, higher frequency movements. To ascertain the amount of temporal information actually encoded by these bands, we applied an SVM classifier to identify the 100 ms period immediately following movement onset.

3.2.2 Detecting movement onset with support vector machine

We performed RBF-kernelized, SVM simulations for onset detection as described in 2.4.7. The values of α selected by the grid search ranged from roughly 10^{-6} to 10^{-2} for the different data

sets, movement types, and brain areas. These values corresponded to as few as 24 and as many as 90 input frequency bands across the 12 channels selected for decoding from MIP or PMd. After parameter selection, we ran the classifier on a disjoint set of test trials for each data set. Recall that for simulation of each session, we fixed the overall false positive rate to 5.0% of total classifications made in the pre-onset period. The true negative rate was then automatically fixed to 95.0%. By adjusting FP rate in this way, the number of positive detections in the onset period was also adjusted, and moreover, the TP rate became the only free variable. Thus, we can directly compare TP rates across sessions.

Figure 10A provides a visual representation of the trial-by-trial classification dynamics in the test set of MIP saccades from M645. In the pre-onset period, red regions correspond to FPs and blue regions to TNs. In the onset period, green regions mark TPs, and yellow regions correspond to FNs, or missed detections. Note that the onset period for each trial is colored fully green or fully yellow, in accordance with the definitions in Table 2B, even though five distinct classifications were made during the interval. For this simulation, the TP rate was 54.3%, as there were 70/129 trials for which at least one onset period positive detection was made. This was significantly higher than chance TP rate (22.6%) at the 95% confidence level (Clopper-Pearson confidence intervals). Chance TP rate was defined as the probability that at least one positive detection would be made during onset period by a naïve classifier for which positive detection rate remains constant for the entire trial. Then $P(TN) = .95 = P(Missed\ Detect)$, and thus,

$$\text{Chance}_{TP} = 1 - P(FN) = 1 - P(Missed\ Detect)^n = .226, \quad (13)$$

where $n = 5$ is the number of SVM classifications that were made during the onset period.

Panel B of Fig 10 shows the normalized distribution of all positive detections from the same simulation, where all positive detections from distinct classifications during onset period are counted individually. The positive detection counts are binned in 100 ms subintervals throughout the pre-onset period, corresponding to four classification times; the onset period bin contains the 100 ms post-onset time, and as such includes a fifth classification time. For each bin, bar height corresponds to its proportion of the total number of positive detections. The blue curve

represents the cumulative proportion of positive detections at 25 ms resolution, and the dashed, black unity line represents the expected cumulative proportion of positive detections for a naïve classifier with a 5.0% positive detection probability at all times in the pre-onset and onset periods. As such, a greater area beneath the dashed line and above the blue curve during pre-onset period corresponds to a more effective detector. In this case, 51.3% of total positive detections were made in the [0, 100] ms onset interval, which comprised 5/41 (12.2%) of all classification times. While the TP rate provides an appropriate evaluation metric for applications in which obtaining at least one true detection in the onset period is most important, the proportion of total true detections relative to FP count is arguably more important for revealing the detector's underlying behavior.

Fig 10, panels C-F each provide the same plot as B, but for pooled detection results across all five sessions for MIP saccades, PMd saccades, MIP pursuits, and PMd pursuits, respectively. In each case, the onset period bin possessed the largest proportion of positive detections: 42.9%, 42.3%, 37.7%, and 34.9%, with only 12.2% of all classification times. Further, the next three largest proportions of (false) positive detections were made, in descending order, in the [-100, 0) ms, [-200, -100) ms, and [-300, -200) ms bins. The distribution of positive detections in the remaining, chronologically earlier bins was approximately uniform in all four cases. Combining the final bin in the pre-onset period with onset period bin, 62.5%, 65.9%, 57.9%, and 57.4% of positive detections were made within 100 ms of movement onset – an interval that accounts for 22.0% of all classification times. All quoted positive detection results for the onset period and for the combined [-100, 100] ms interval are significant at the 95% confidence level (Clopper-Pearson confidence intervals). However, as is apparent in Fig 10A, many trials for which positive detections were made in the onset period also had false positives in the late pre-onset period. In other words, the large proportion of positive detections made near movement onset does not imply that the detections were distributed uniformly – or close to uniformly – across all trials within a session.

For MIP saccades, PMd saccades, MIP pursuits, and PMd pursuits, Figure 11 shows the pooled TP rate for trials across all sessions. Error bars denote the 95% Clopper-Pearson confidence intervals. The pooled TP rates for all four cases were significantly above chance (22.6%, as

derived in (13)), with respective values of 44.5%, 43.0%, 39.9%, and 36.2%. The MIP and PMd saccade TP rates were not significantly different from each other, nor were the MIP and PMd pursuit rates. In both MIP and PMd, the saccade TP rate was significantly higher than the pursuit rate.

4. Discussion

In chapter 3, we first showed that saccade and pursuit movement direction is encoded in medial intra-parietal (MIP) and dorsal pre-motor (PMd) local field potentials (LFPs) during reach planning. Using LFP spectral power, we also demonstrated that saccade and pursuit onset can be decoded with a causal support vector machine (SVM) detector. In this chapter, we discuss these results in the context of previous studies. We also analyze our methods and suggest related future work. Section 4.1 focuses on direction decoding and section 4.2 on movement detection.

4.1 Eye movement direction decoding

To decode eye movement directions in the reach-memory (T1), pre-onset (T2), peri-onset (T3), and post-onset (T4) periods of each trial, we first identified directionally tuned frequency bands from the training set. Using spectral power from the tuned bands, we then applied a naïve Bayes classifier (NBC) to decode eye movement direction of the test trial in each period. We discuss frequency band directional tuning, as determined from ANOVA, in 4.1.1, and implications of the NBC decoding in 4.1.2.

4.1.1 Eye movement directional tuning

To our knowledge, this was the first investigation of eye movement encoding in LFPs recorded during reach planning. Although, our capacity to directly compare results is accordingly limited, other groups have studied similar problems.

Scherberger and collaborators recorded MIP LFPs from a macaque that was instructed to execute either a delayed reach or a delayed saccade – but never both in the same trial [31]. During saccade planning, the number of channels they observed with directional tuning in frequency bands between 0-100 Hz closely resembled the distributions we observed for cis-directional saccades during the pre- and peri-onset periods (top row of Fig 4). Notably, the distribution they

observed during reach planning was very similar to the saccade planning distribution. This could hint that the MIP LFPs encode a cognitive goal variable, like target location, as opposed to movement-specific trajectories. To further endorse this point, the MIP distributions we observed for cis-directional pursuits in exclusive sessions (third row of Fig 4), and cis- and trans-directional saccades in inclusive sessions (top row of Fig 5), were also similar. Conversely, the distribution for trans-directional pursuits (third row of Fig 5) featured much more tuning below 15 Hz and much less in the 15-35 Hz bands. This elevated, low frequency tuning could represent increased coordination between cortical areas; this matches theory suggesting the brain behaves as a low-pass filter, using high frequency oscillations to communicate locally and slower variations to transmit across longer distances [27]. Increased coordination may have been required since the two extended movements – pursuit and reach – were being simultaneously planned, and were then executed in quick succession. The lack of low frequency tuning for trans-saccades could be explained by their more rapid, and thus higher frequency, nature. In any case, future work is required to determine whether specific frequency bands, within each channel, are tuned for more than one of the saccade, pursuit, or reach movement types.

4.1.2 Eye movement direction decoding

We used a naïve Bayes classifier to extract tuning information from the frequency bands by decoding saccade and pursuit movement direction. Our results, reported in section 3.1.2, demonstrated that LFP spectral power from MIP and PMd encodes both saccade and pursuit direction during reach planning. Previous studies have also decoded eye movement direction from areas MIP and PMd using a naïve Bayes classifier [31,91]. A recent study by Freidman demonstrated that saccade and pursuit direction, as well as pursuit trajectory, can be decoded from the spike signal of an ensemble of MIP and PMd neurons [91]. Moreover, Freidman's study used the same paradigm as the present work, in which eye movements were made during a reach planning period. Scherberger and collaborators used MIP LFP spectral power to decode saccade direction, but no reach was planned during, nor made after, saccade execution [31]. These studies provided the foundation for our hypothesis that eye movement direction is encoded in the LFP during reach planning. However, since the LFP signal is primarily composed of synaptic inputs,

while the spike signal mainly consists of pyramidal cell output, and because MIP and PMd are reach-specific areas, it was not previously clear that such encoding exists.

The methods we used for decoding were primarily meant to establish the existence of eye movement direction tuning that is independent of reach direction tuning in LFP spectral power. As such, strong conclusions cannot be drawn from comparisons to other studies that aimed to optimize decode rate. However, the difference in decode rates between our study and the Scherberger [31] and Friedman [91] studies is notable. Scherberger and collaborators reported a 40.1% direction classification rate from their simulations of an eight target, center-out delayed saccade task (12.5% chance). Their predictions used LFP spectral power recorded during a saccade planning period, roughly equivalent to our T2, pre-onset period. Using spike signals from a pre-onset period, Friedman achieved an approximately 50% direction classification rate (20% chance; four target center-out task, plus fixation trials with no eye movement). Relative to chance, these rates were much more significant than the MIP saccade decode rates we achieved with simulations of either the exclusive or inclusive datasets. The contrast with the Scherberger results could indicate that the simultaneous reach planning partially obfuscates the eye movement direction tuning. This would not be surprising, given central the role of MIP as a reach area. The discrepancy with the Friedman results could be due to superior spatial resolution attainable by from the spikes of individual neurons. While a number of neurons may be encoding eye movement direction, the summative and less spatially concentrated LFP could be overwhelmed by a larger fraction of neurons encoding reach movement direction, or other reach variables. The same effects would likely be present in PMd, given its similar functional role and the comparable decode rates we achieved for saccades and pursuits.

Significant modifications to the NBC algorithm (2.4.4-2.4.5) are required to maximize the eye movement direction decode rate. Most simply, a parameter selection and cross-validation pre-processing step – similar to the one described in 2.4.8 for the onset detector – to determine an optimal ANOVA p-value threshold could be added. This would provide an empirical method for the balancing the trade-off between information quality and quantity from frequency bands to be used for decoding. Figure 3 provides an example of this balance. The tuning curve for the first frequency band (plot A, right panel) – 105-125 Hz, channel 1 – suggests it was highly

informative regarding whether a given saccade was made in the upward direction. Conversely, the tuning curve for the second band (plot B, right panel) – 45-55 Hz, channel 17 – suggests it was much less informative, as the mean power for each direction fell within the standard deviation of the mean for every other direction. Over a large number of trials, the second band could still provide statistically significant tuning information, but it may not be helpful for accurate decoding on a single-trial basis. Applying a more sophisticated classifier than the NBC would likely help decoding efficiency as well. While not as entrenched in the literature, recent studies have shown that SVMs, artificial neural nets, and other modern learning algorithms have modestly outperformed the naïve Bayes in similar decoding tasks [115,116]. Finally, decoding could likely be improved with the inclusion of more input data. For mainly computational reasons, we limited each simulation to 12 input channels, exclusively from either MIP or PMd. However, other studies have shown improved decoding by increasing the number of input channels [117], using channels recorded simultaneously from different locations (i.e. MIP and PMd) [15], and using spike and LFP data together [11,118]. Since we have established that eye movement direction is encoded in MIP and PMd LFP spectral power, improvements like these will be necessary to better gauge the utility of the encoding, and to attain a level of accuracy that could be useful for a clinical prosthetic system.

4.2 Eye movement onset detection

The second objective of this study was to develop and implement a strategy for detecting eye movement onset time from LFP spectral power in MIP and PMd. In an MIP LFP reach-prosthetic study [119], Hwang and Andersen exploited strong and consistent modulations in low-frequency spectral power to detect arm movement onset. By comparing a difference in the time-derivative of power in two frequency bands, they created a threshold-based “Go” signal. Unfortunately, no such strong and consistent modulations exist for eye movement onset, as is apparent from Figure 2C. Therefore, we proposed and implemented a more general approach for eye movement onset detection, as detailed in 2.4.6-2.4.8.

4.2.1 Eye movement temporal tuning

We first used ANOVA to identify frequency bands in the LFP spectral power that were modulated by eye movement onset. Previous studies of posterior parietal cortex (PPC) LFP temporal dynamics during saccade tasks reported findings that overlap with ours. Scherberger and collaborators studied spectral power modulations near saccade onset [31], in addition to decoding movement direction, as covered previously. They compared spectral power signals from saccade planning and execution periods, and found the largest onset-tuned modulations were in the 5-15 Hz and 35-65 Hz frequency ranges. The latter range is consistent with our ANOVA results (Figure 9A), but we observed very little significant temporal tuning below 15 Hz. One explanation for this discrepancy relates to our procedure: we obtained average power values using the three data windows ending in each of the [-150, -100] ms and [50, 100] ms subintervals, from the pre-onset and onset periods, respectively. The middle windows from the subintervals were, therefore, separated by 200 ms. This length of time corresponds to the period of a single 5 Hz cycle, or just three 15 Hz cycles; in contrast, seven 35 Hz and sixteen 80 Hz cycles can be completed in the same time. As a result, there may have been an insufficient amount of time for significant, low-frequency modulations to appear in the log-power estimates ($p < 0.001$; ANOVA), and thus the histogram of Fig 9A. A second LFP-saccade study [59] – which recorded from the lateral intra-parietal cortex of the PPC – also reported temporal information encoded in LFP spectral power below 20 Hz. The blindness of our methodology to these potentially rich sources of onset-tuning represents a significant problem for which future studies should account. An important first step will be to identify the extent to which the problem is systematic – for which some form of estimate re-scaling or shift in the ANOVA subinterval times could improve results – versus random variance – for which changes to the spectral estimation procedure, such as increasing the window length, could be required.

For the present thesis, Figure 10 aids in the evaluation of our algorithm, and specifically the choice of using the [-150, -100] ms subinterval for ANOVA input. The three windows ending in this subinterval were centered at -300 ms, -275 ms, and -250 ms relative to eye movement onset. Fig 10, panels C-F show that for saccades and pursuits, decoded from MIP and PMd, the proportion of false positive detections was smaller in all 100 ms bins in the [-900, 300] ms

interval than in any of the bins in the [-300, 0) ms interval. Therefore, the decision to use ANOVA to identify spectral power frequency bands that discriminate between the late pre-onset and onset periods was appropriate. Including earlier times would be unlikely to significantly improve performance, since in all four cases, bins in the [-900, -300) ms interval never comprised more than 5% of the total positive detections. Shifting the subinterval to include times closer to eye movement onset could lead to modest performance improvements, but would also lead to greater overlaps with the onset period data. The lack of sharp spectral features near movement onset, as shown in Figure 2C, means that the number of significantly tuned bands rapidly declines as the pre-onset and onset ANOVA subintervals approach one another. Since the ANOVA procedure only facilitates feature selection, aggressively eliminating many frequency bands would likely be detrimental to the final decoding. Ultimately, rigorous cross-validation over candidate subintervals should be applied to optimize onset-tuned frequency band selection.

4.2.2 Eye movement onset detection

In both studies discussed in 4.2.1 [31,59], the authors performed post-hoc analyses to investigate temporal onset-tuning and classify LFP spectral power data windows as either pre- or post-onset. More specifically, they used knowledge of the actual eye movement onset time to differentiate and label pre- and post-onset signals before beginning their decoding. Accordingly, they were able to convincingly show that PPC (MIP and LIP) LFP spectral power is well-suited to discriminating between behavioral states; Scherberger and collaborators classified baseline, pre-onset, and post-onset windows with less than a 10% error rate using 20 or fewer LFP channels [31]. However, since they used information that would not be available in real-time (i.e. the movement onset time), their methods have little direct predictive power. To simulate real-time eye movement onset detection, we implemented an SVM to make causal predictions of whether data windows belonged to the pre-onset period or the onset period.

Our SVM onset detection algorithm achieved true-positive rates that were significantly above chance for saccades and pursuits, recorded from MIP and PMd (see Figure 11). This result demonstrates that saccade-related behavioral state information encoded in the MIP and PMd

LFPs, as reported in previous studies [31,59], can be exploited to detect movement onset in real-time. To our knowledge, this is the first work to do so using LFPs from reach areas; however, other eye movement timing-based studies have shown that saccade onset can be reliably identified using spike signals from oculomotor areas like FEF and SEF [120]. For motor prosthetic systems, it is undesirable to record from areas that are not strongly reach-related. As such, the results presented here are significant, despite not yet attaining a level that could immediately improve a prosthetic system.

Beyond the simple TP rates reported in Fig 11, the pooled distributions of positive classifications depicted in Figure 10, panels C-F, reveal important trends. In 3.2.2, we noted that between 57.4% (PMd pursuits) and 65.9% (PMd saccades) of all positive classifications, true or false, were made within 100 ms of actual onset time across all data sets. Going back further, between 79.5% (MIP saccades) and 85.3% (PMd pursuits) of positive classifications were made in the [-300, 100] ms interval, which represented just 17/41 (41.4%) of the times examined for each trial. Meanwhile, the fixation target prompted saccades between 170 ms and 357 ms before onset (mean: 221 ms) and pursuits between 131 ms and 366 ms before onset (mean: 224 ms). The movement cues were, therefore, being processed at times coinciding with the observed increase in false positives. This is further evidence of the temporal sensitivity to behavioral state in MIP and PMd. Fig 10A – which has qualitatively similar dynamics to other plots of the same type across different sessions and movement types – provides further insight regarding the false positive distributions. There were few cases, especially near movement onset, of just one positive detection occurring without more following in close proximity. In other words, on a single trial basis, errors were more likely due to a systematic offset in the signal than to random fluctuations in LFP spectral power. This could be construed as positive – the problem is well-posed, such that small changes in time correspond to small changes in spectral power, and thus similar classifications at neighboring times. Conversely, it illuminates a potential difficulty for attaining high temporal precision. Introducing a normalization to better evaluate the spectral power distribution across frequency bands or across time could mitigate the impact of systematic errors. Identifying an effective normalization scheme could also improve understanding of how temporal information for eye movements is encoded in the LFP. Finally, to improve precision and overall performance of the detector, more significant changes to the algorithm may be

necessary. Within the SVM framework, incorporating additional features would be straightforward. For example, windowed spike counts from neurons that are recorded simultaneously with the LFP could provide more granular information without requiring further surgery or hardware; theory for incorporating the two signal types is already under development [11,118,121]. However, even with a simple and general method for feature selection from LFP spectral power, we were able to decode eye movement onset time significantly above chance for saccades and pursuits, with data from both MIP and PMd.

5. Conclusions and neural prosthetic applications

In summary, the two novel objectives of this thesis were:

- i) To determine the existence of saccade and pursuit directional encoding in LFP spectral power from areas MIP and PMd during reach planning;
- ii) During reach planning, to determine the existence of temporal oculomotor information encoded in MIP and PMd LFP spectral power, and leverage it to detect saccade and pursuit movement onsets.

Throughout this study, we found strong similarity between the results for saccades and pursuits, in both MIP and PMd. This was notable, but not necessarily surprising given the overlapping mechanisms and purposes underlying saccades and pursuits, as well as the functional similarities between sensorimotor areas MIP and PMd. Our methodology was not designed to draw direct comparisons between movement types and brain areas, but the overarching results of this work apply similarly to all cases.

For objective i), we showed that eye movement direction is encoded by LFP spectral power. However, our modest decode rates suggest that LFPs may provide insufficient neural resolution to obtain optimal decoding during reach planning. Since the primary reason to decode eye movement variables from MIP and PMd is for motor prosthetic application, a more sophisticated decoding algorithm will be required to gauge potential for clinical utility.

For objective ii), we detected saccade and pursuit onset at 100 ms temporal resolution using a simple spectral power feature selection process, paired with a support vector machine classifier. While MIP and PMd LFPs may not provide the same temporal precision as oculomotor-specific areas (e.g. [120]), a refined version of our algorithm could eventually aid motor prosthetic systems. For example, once eye movement onset is detected, a movement direction or target decoder can be queried to update eye position variables. Since reach target is encoded relative to

eye position in both MIP and PMd, accurate knowledge of eye position enables improvements to reach accuracy as well.

6. Figures

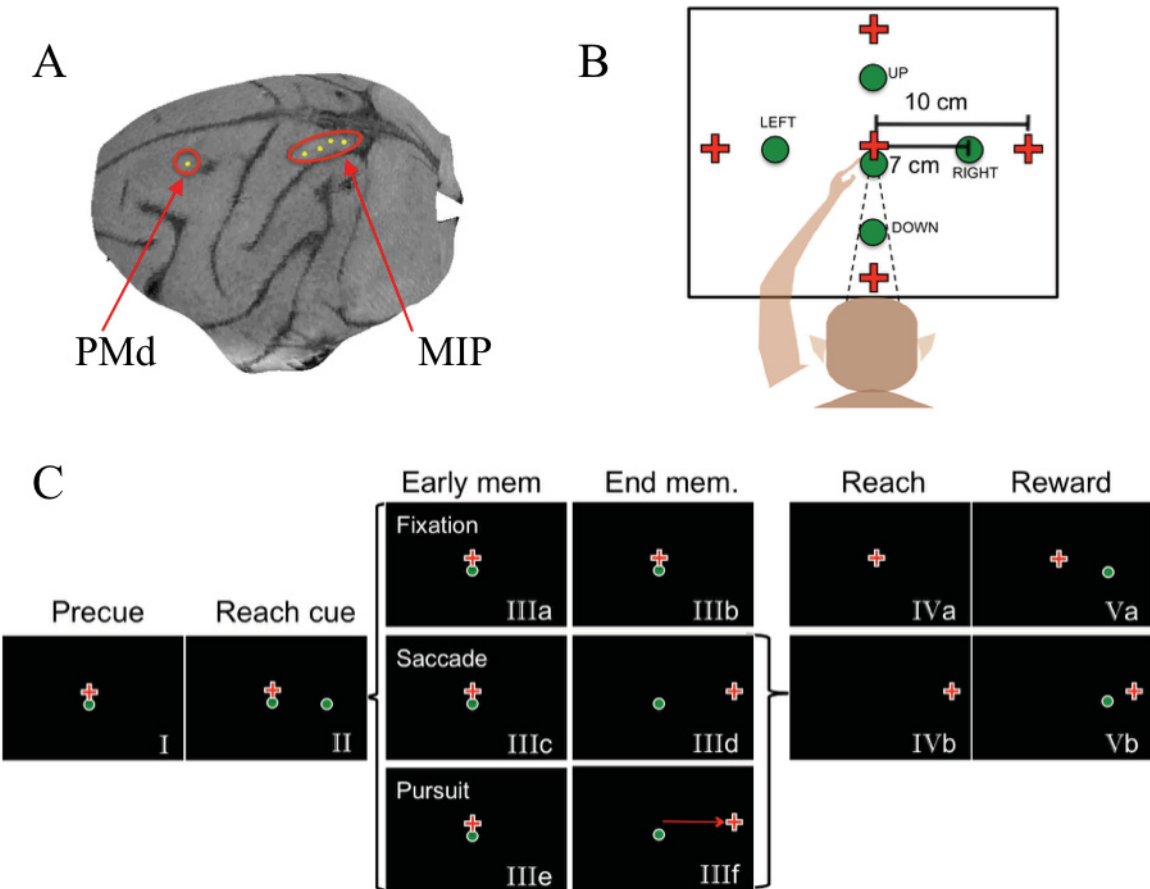


Figure 1 (reproduced with permission from Stacey, 2015): Center-out look-reach experiment paradigm. (A) Areas MIP and PMd in the macaque cortex. Four 16-channel electrode arrays were implanted in MIP, and one 32-channel array was implanted in PMd. Approximate locations represented by yellow dots; (B) Diagram of possible gaze (red cross) and touch (green circle) target locations. The subject began each trial by fixating and touching the central targets with all other targets extinguished; (C) Schematic for the behavioral task performed by the macaque subject (see 2.3 for in-depth description). Red crosses and green circles represent fixation and touch targets, respectively, as in (B).

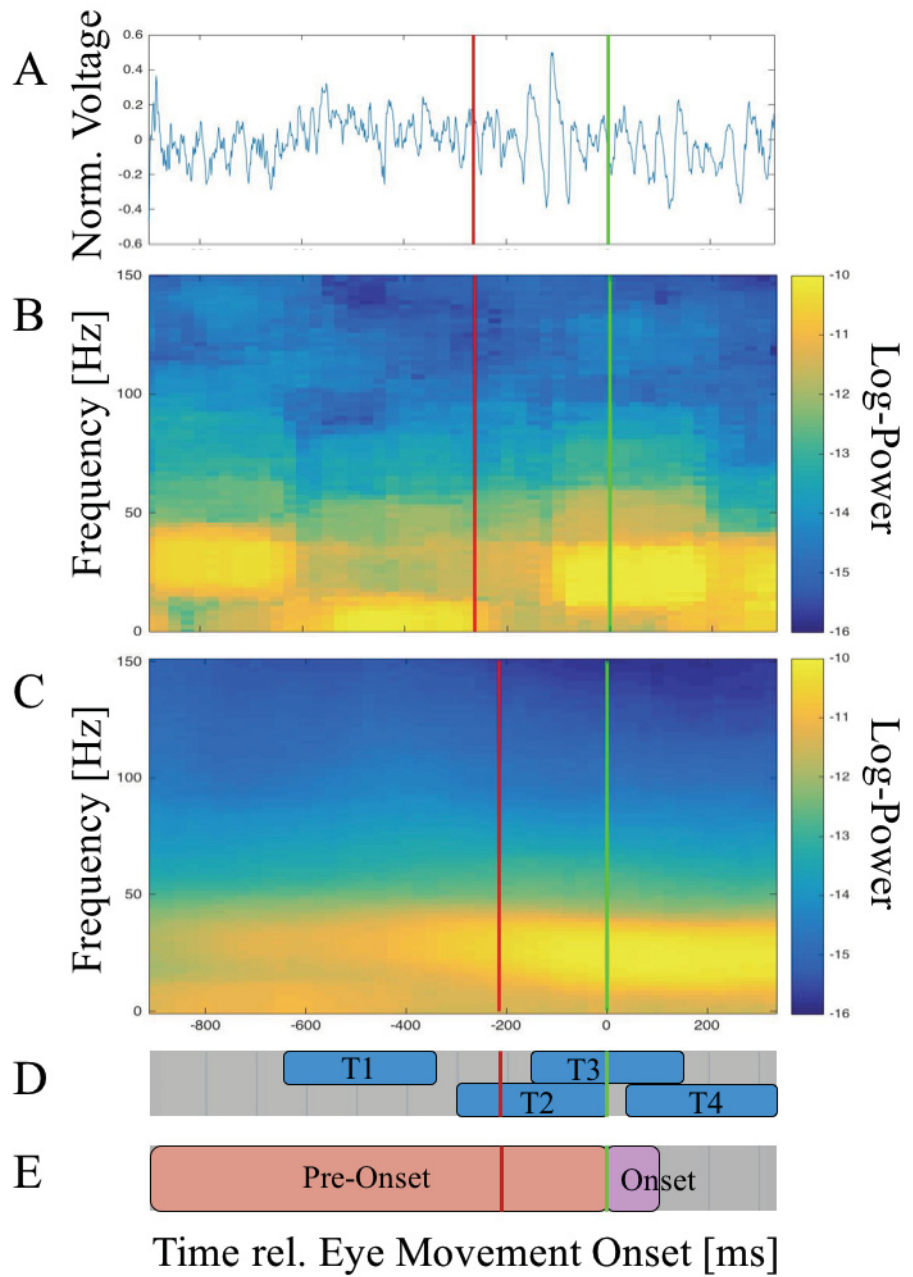


Figure 2: (A) Normalized, single-channel LFP time series recorded from area MIP during a cis-directional, rightward saccade trial. Red line marks eye movement cue time, and green line marks eye movement onset; (B) Log-power spectrogram produced from the LFP time series in (A). Horizontal axis times correspond to end of data windows, such that all estimates are causal; (C) Averaged log-power spectrogram for all rightward saccade trials from session M645. Red line marks median eye movement cue time; (D) Locations of reach-memory (T1), pre-onset (T2), peri-onset (T3), and post-onset (T4) periods for eye movement direction classification; (E) Locations of pre-onset and onset periods for eye movement onset classification.

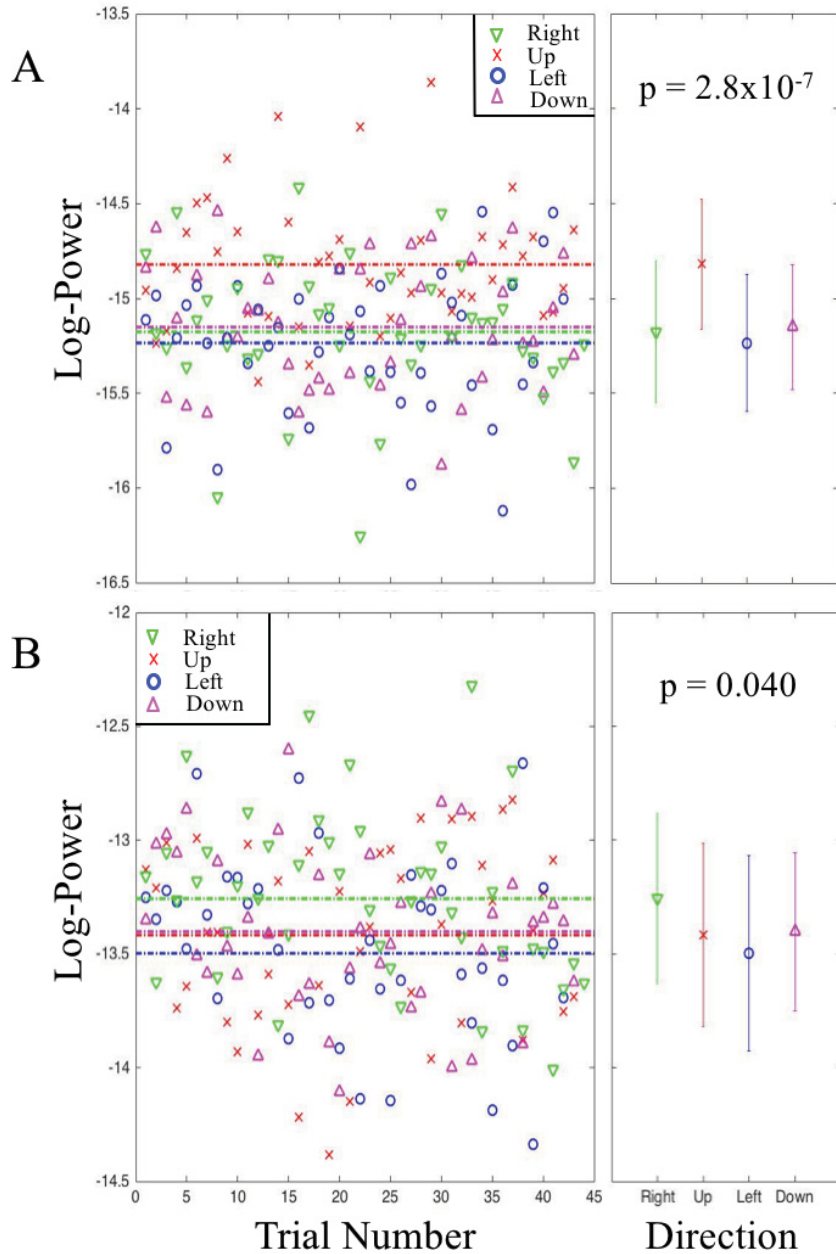


Figure 3: (A) Left panel shows scatter plot of channel 1, 105-125 Hz frequency band log-powers during peri-onset period (T3) from saccade trials in session M645. According to ANOVA this was the band tuned at the highest confidence ($p = 2.8 \times 10^{-7}$). Inverted green triangles correspond to rightward saccade trials, red crosses to upward, blue circles to leftward, and magenta triangles to downward. Dashed, horizontal lines mark mean log-powers of respectively colored data-points. Right panel shows mean log-powers, plus or minus standard deviation, for each direction; (B) Same as (A), with data from channel 17, 45-55 Hz frequency band. According to ANOVA, this band narrowly achieved the criterion necessary to be classified as significantly directionally tuned (($p = 0.04 < \alpha = 0.05$)).

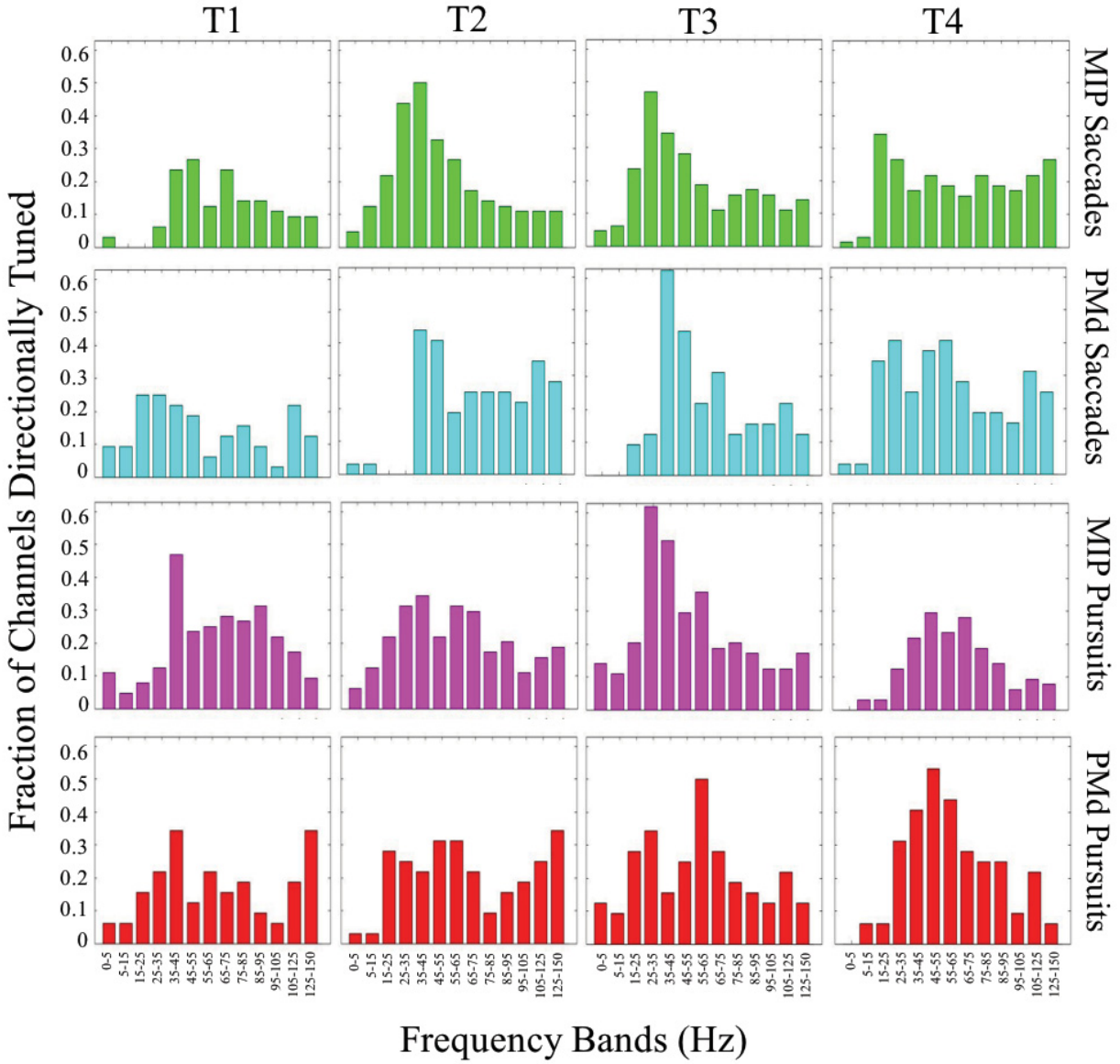


Figure 4: Directional tuning histograms from the two exclusive datasets, such all trials featured cis-directional eye movements and reaches. The panels show the fraction of channels that were significantly directionally tuned ($p < 0.05$; ANOVA) in each LFP spectrogram frequency band. In total there were $2 \times 32 = 64$ MIP channels and $2 \times 16 = 32$ PMd channels. From left to right, columns correspond to data from the reach-memory period (T1), movement cue period (T2), peri-onset period (T3), and post-onset period (T4). See Table 1 for further description of T1-T4. From top to bottom, panel rows correspond to MIP data for saccades, PMd data for saccades, MIP data for pursuits, and PMd data for pursuits.

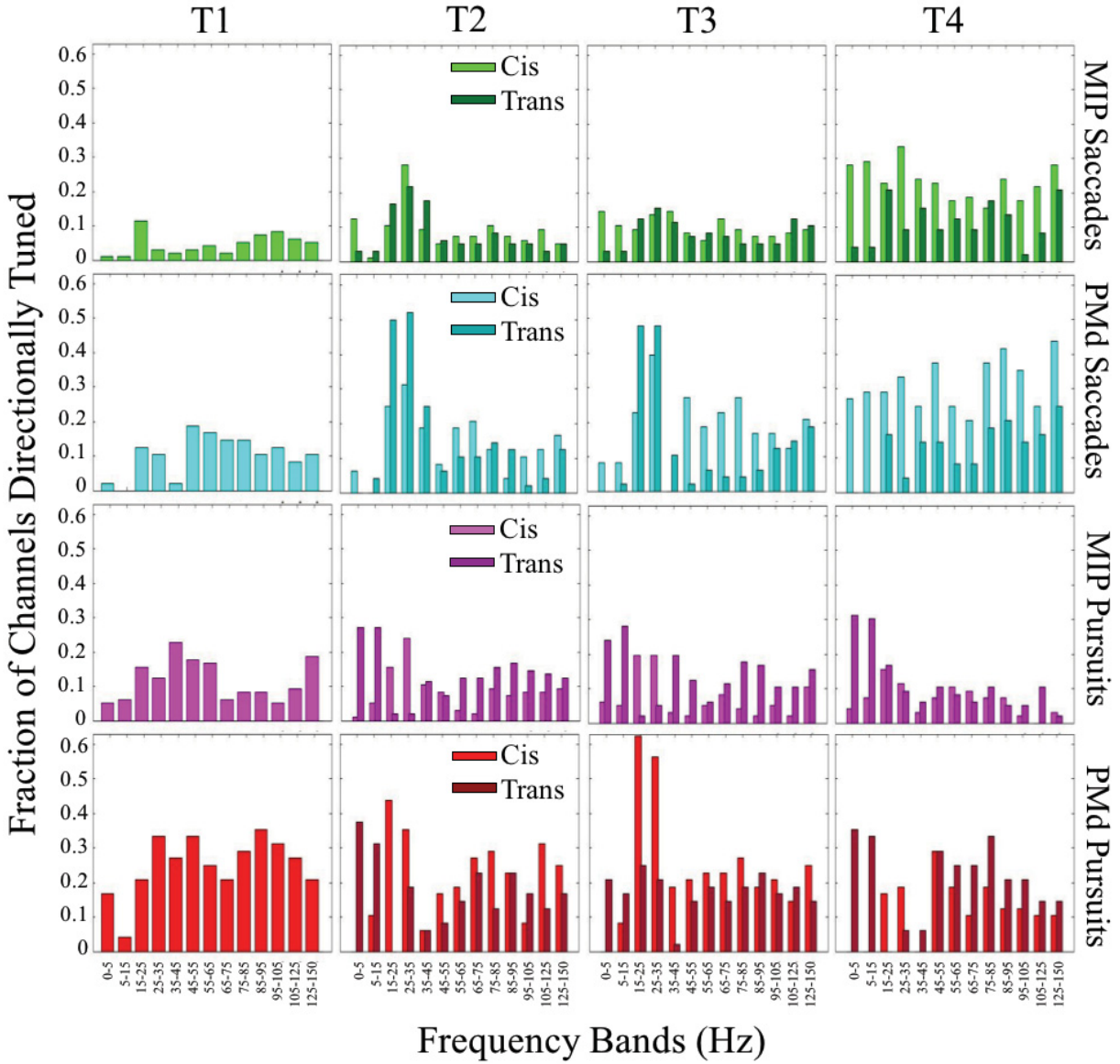


Figure 5: Directional tuning histograms from the three inclusive data sets with cis- and trans-directional trials. The panels show the fraction of channels that were significantly directionally tuned ($p < 0.05$; ANOVA) in each LFP spectrogram frequency band. The lighter bars on the left side of each pair correspond to cis trials and the darker bars on the right correspond trans trials. In total there were $3 \times 32 = 96$ MIP channels and $3 \times 16 = 48$ PMd channels. From left to right, columns correspond to data from the reach-memory period (T1), movement cue period (T2), peri-onset period (T3), and post-onset period (T4). See Table 1 for further description of T1-T4. From top to bottom, panel rows correspond to MIP data for saccades, PMd data for saccades, MIP data for pursuits, and PMd data for pursuits. Trans tuning results were not included for T1 because there was no fixed relationship between reach and eye movement directions. Therefore, any detected tuning during this period would be spurious.

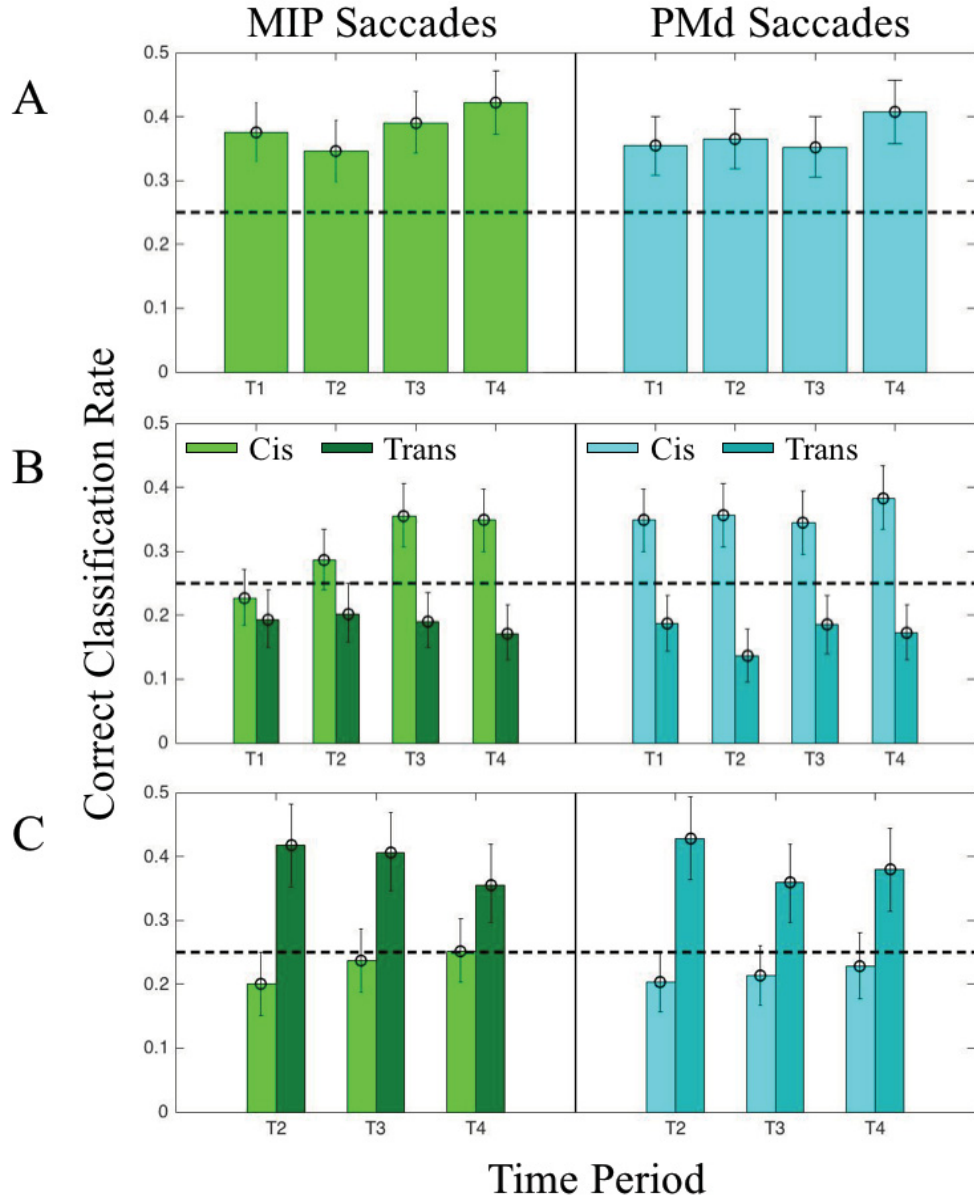


Figure 6: Correct direction decode rates for saccades during time periods T1-T4 (see Table 1 for description). In panels (A)-(C), decoding results from MIP are shown on the left side, decoding results from PMd are shown on the right. Dashed, horizontal line represents chance correct classification rate (25%). Error bars are 95% confidence intervals computed with Monte Carlo bootstrap resampling; (A) Classification rates for cis-directional trials from pooled, exclusive datasets; (B) Classification rates for cis- and trans-directional trials from pooled, inclusive datasets, using *only cis-directional trials* to train the classifier. Lighter bars on left in each pair correspond to cis decode rates, and darker bars on right correspond to trans decode rates; (C) Same as (B), except classifier was trained using *only trans-directional trials*. Rates for memory period T1 are not shown since eye movement had not been cued and its direction relative to planned reach direction was not controlled for.

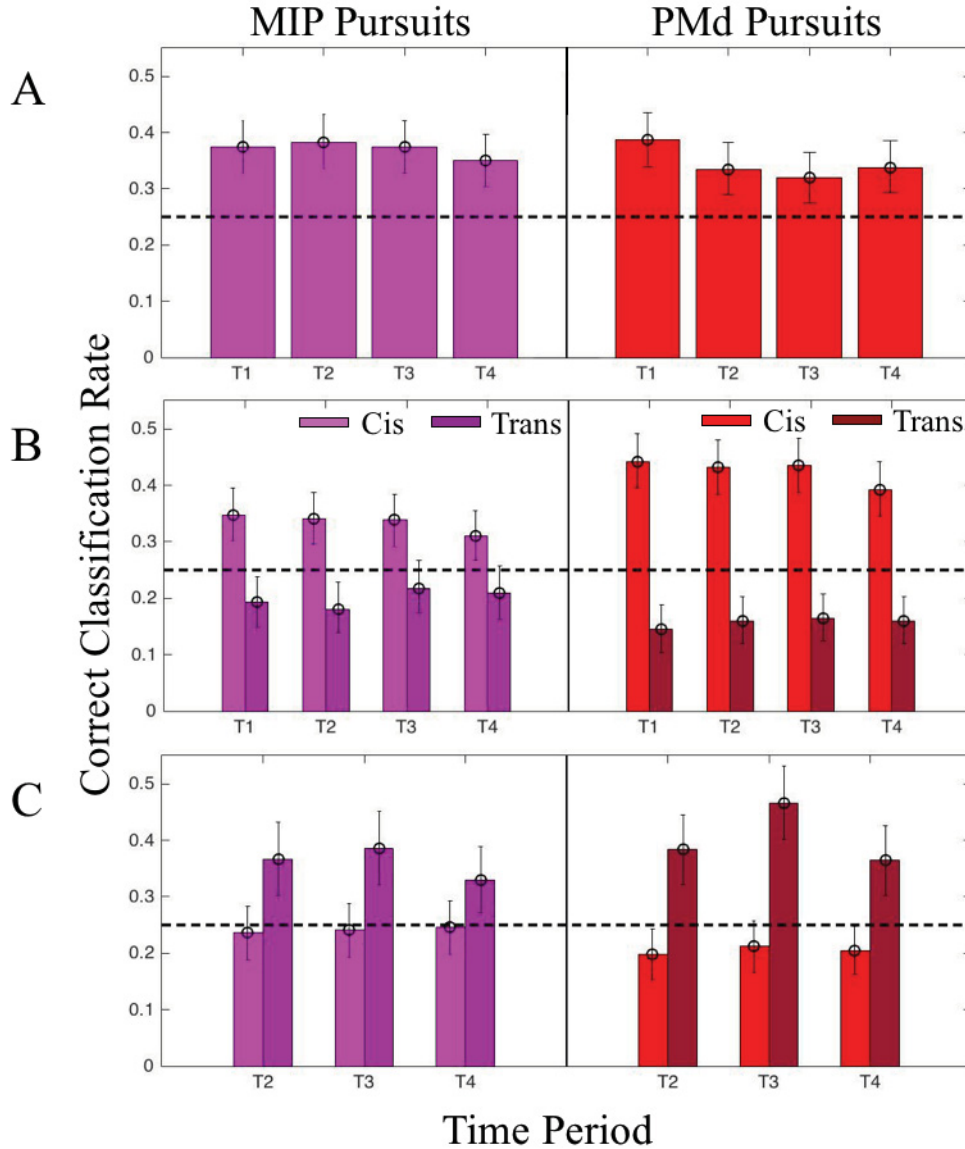


Figure 7: Correct direction decode rates for pursuits during time periods T1-T4 (see Table 1 for description). In panels (A)-(C), decoding results from MIP are shown on the left side, decoding results from PMd are shown on the right. Dashed, horizontal line represents chance correct classification rate (25%). Error bars are 95% confidence intervals computed with Monte Carlo bootstrap resampling; (A) Classification rates for cis-directional trials from pooled, exclusive datasets; (B) Classification rates for cis- and trans-directional trials from pooled, inclusive datasets, using *only cis-directional trials* to train the classifier. Lighter bars on left in each pair correspond to cis decode rates, and darker bars on right correspond to trans decode rates; (C) Same as (B), except classifier was trained using *only trans-directional trials*. Rates for memory period T1 are not shown since eye movement had not been cued and its direction relative to planned reach direction was not controlled for.

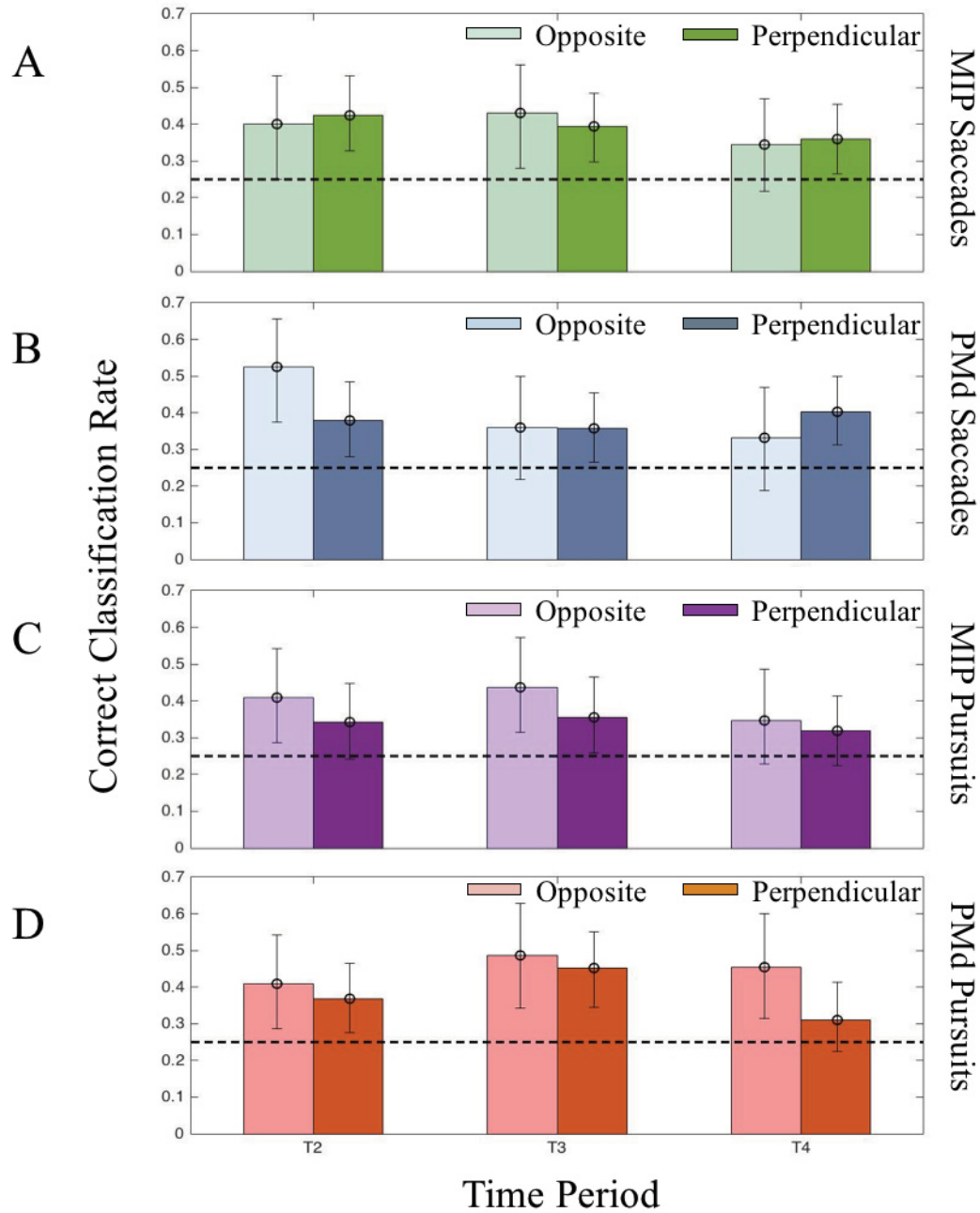


Figure 8: Correct direction decode rates for trans-directional eye movements from pooled, inclusive datasets during time periods T2-T4 (see Table 1 for description), with classifier trained on only trans trials; (A)-(D) Decode rates for opposite-trans (light colored) and perpendicular-trans (dark colored) trials, for MIP saccades, PMd saccades, MIP pursuits, and PMd pursuits, respectively. Dashed, horizontal line represents chance classification rate, and error bars are 95% bootstrap confidence intervals.

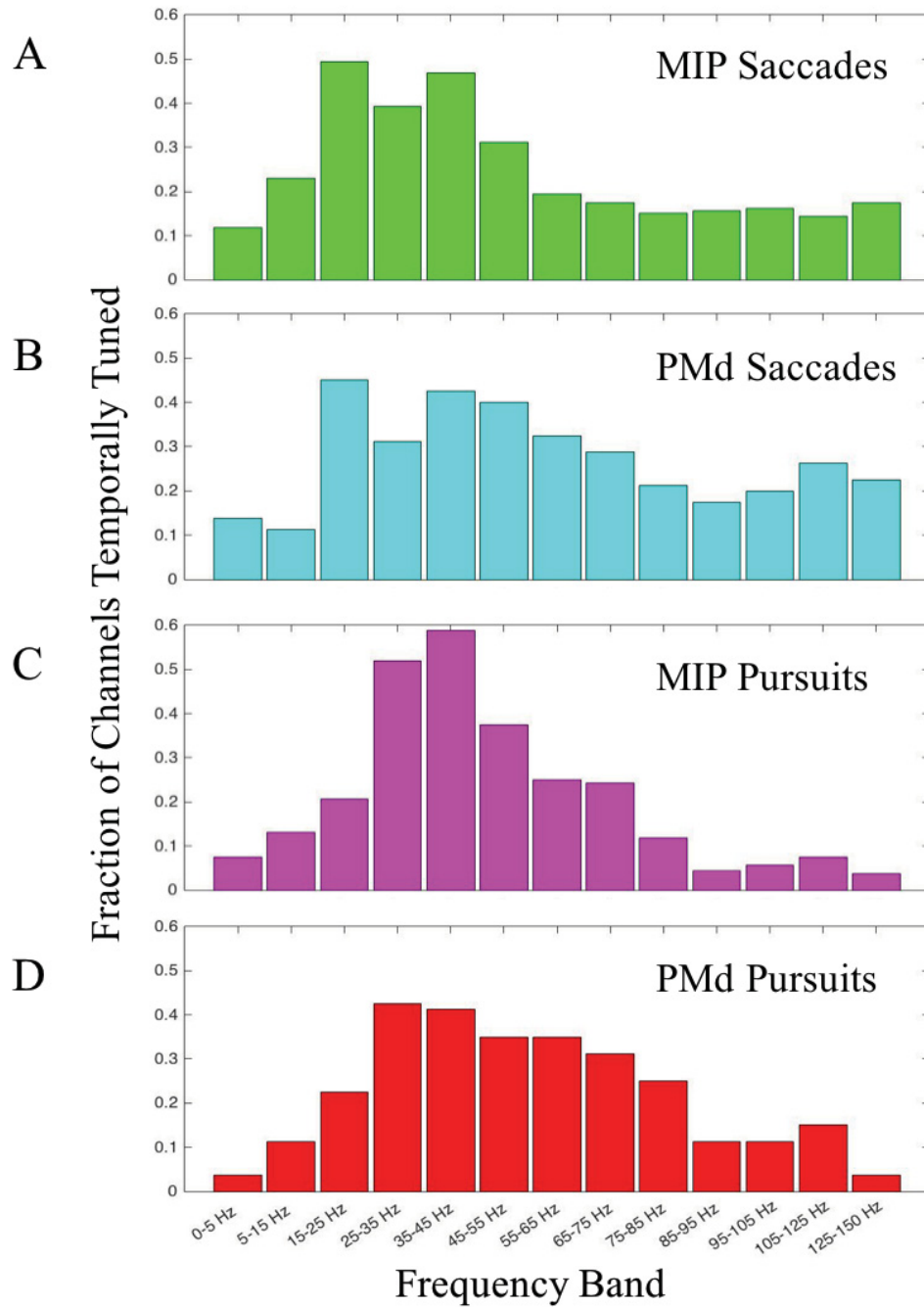


Figure 9: Normalized temporal tuning histograms across all data sets. A channel was considered temporally tuned if ANOVA yielded a p-value of $p < 0.001$, reflecting confidence that log-LFP power in the band was modulated by movement onset. Specifically, average log-power from intervals [-150, -100] ms and [50, 100] ms relative to movement onset in each trial were compared with ANOVA (see 2.4.3 and 2.4.6); (A) Data recorded from MIP during saccade trials; (B) Data from PMd during saccades; (C) Data from MIP during pursuits; (D) Data from PMd during pursuits. In total $5 \times 32 = 160$ MIP channels and $5 \times 16 = 80$ PMd channels were used.

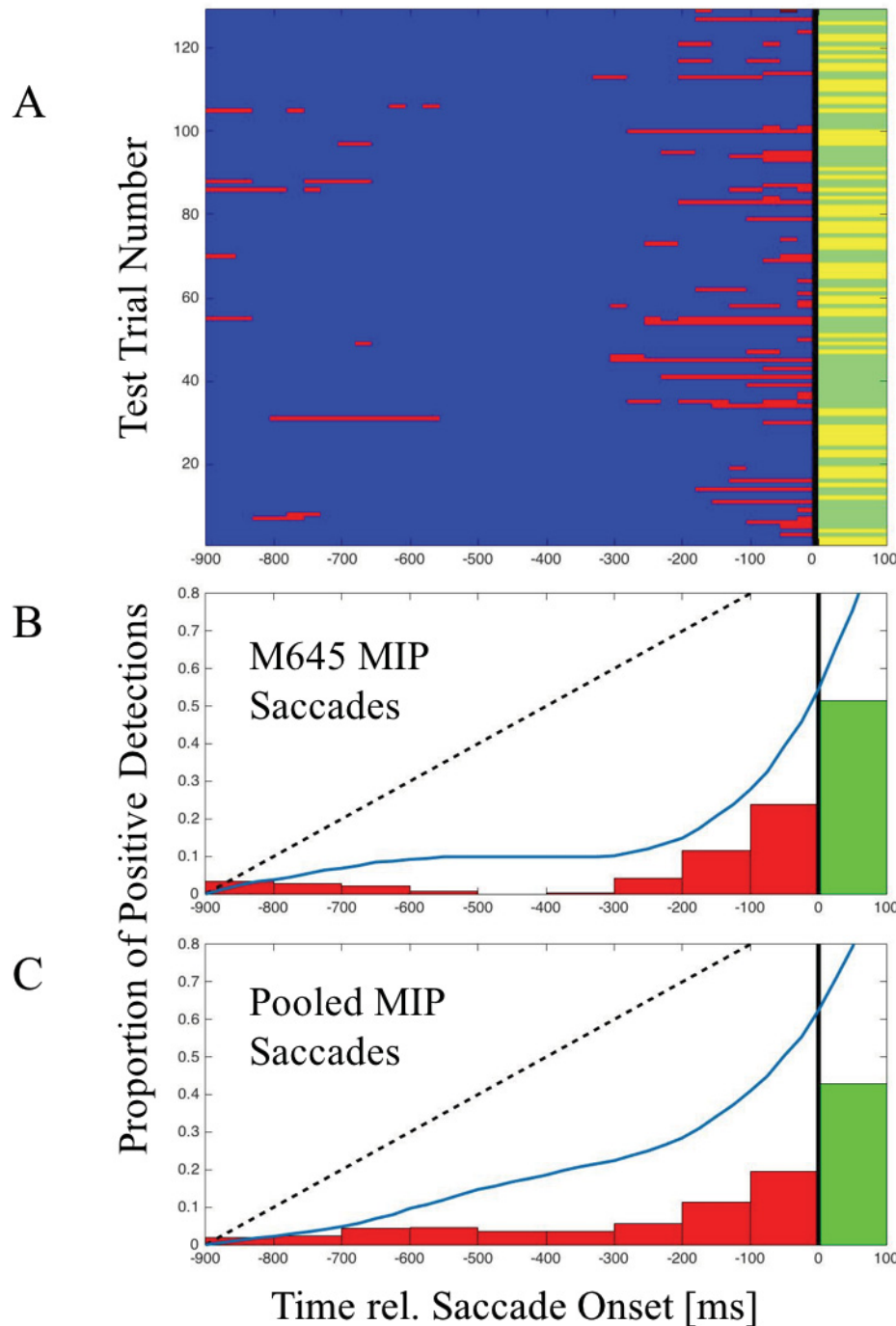


Figure 10: SVM eye movement onset detection; (A) Visual representation of saccade onset detection results by test trial (vertical axis) for MIP data from session M645. Red regions in the pre-onset period, $[-900, 0]$ ms, correspond to false positive detections, which were fixed to a 5.0% rate across all trials in each data set. Blue regions correspond to true negatives (equivalently fixed to 95.0%). Green regions in the onset period, $[0, 100]$ ms, correspond to true positive (TP) detections, and yellow regions correspond to false negatives (FNs). There was

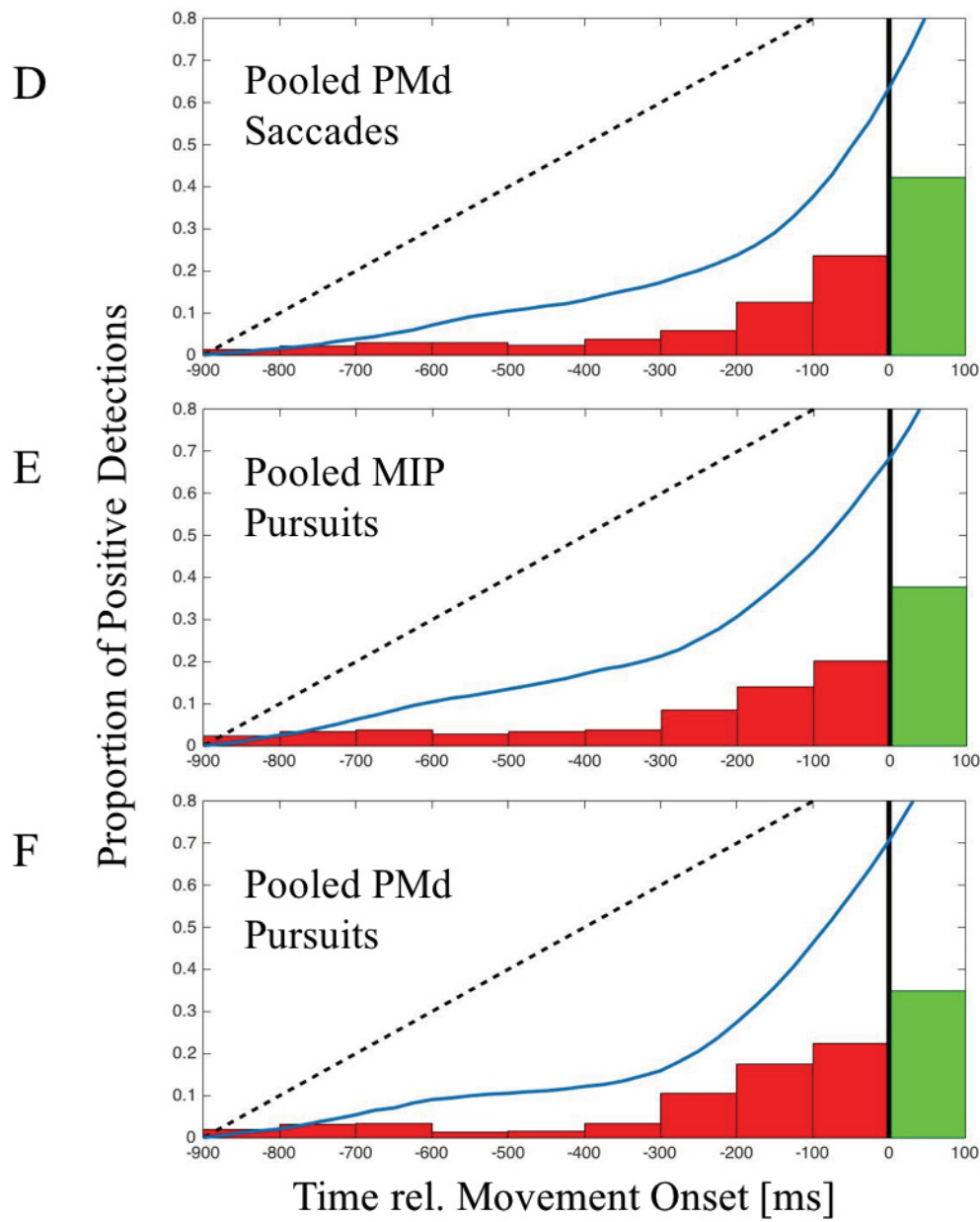


Figure 10 (cont.): either one TP or one FN per trial; see Table 2B for complete description; (B) Normalized distribution of positive detections for results shown in (A), binned by 100 ms intervals. Unlike in (A), every positive detection in the onset period was counted individually for fair comparison to false positive detections. Blue curve shows cumulative proportion of positive detections at 25 ms resolution, and dotted black unity line represents cumulative proportion of positive detections for an idealized simulation in which positive detections are uniformly distributed; (C)-(F) Same as (B) with results pooled across all data sets, corresponding to MIP saccades, PMd saccades, MIP pursuits, and PMd pursuits, respectively.

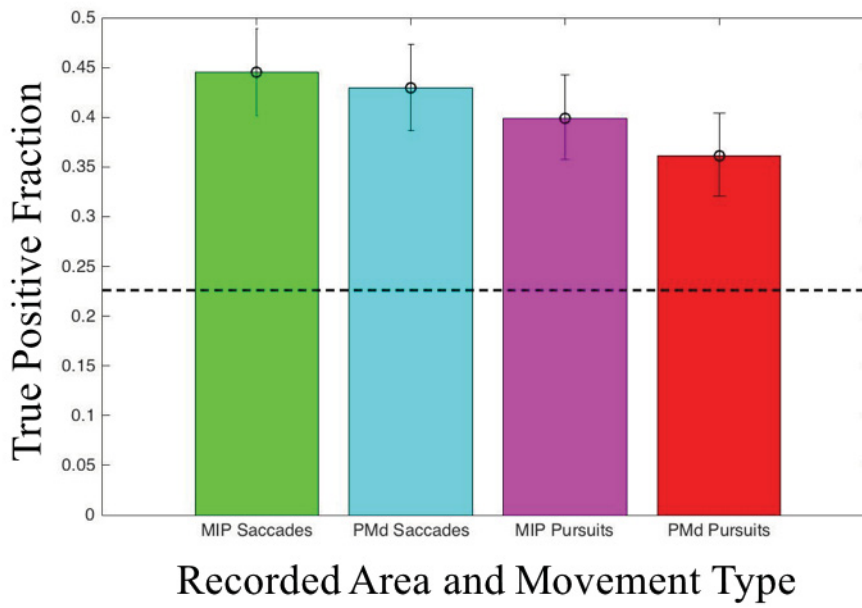


Figure 11: True positive (TP) detection rates by recorded brain area and movement type, pooled across all five datasets. False positive rate was fixed to 5.0% for each dataset individually, and results across all datasets were averaged, with weighting by number of trials. Error bars are 95% Clopper-Pearson confidence intervals. Dashed black line represents TP chance rate of 22.6%, as derived in equation (13).

7. References

- [1] B. Thylefors, "A global initiative for the elimination of avoidable blindness", *Amer. J. Ophthalmology*, vol. 125, no. 1, pp. 90-93, 1998.
- [2] R. Mitchell, "How many deaf people are there in the United States? Estimates from the survey of income and program participation", *J. Deaf Studies Deaf Education*, vol. 11, no. 1, pp. 112-119, 2005.
- [3] K. Ziegler-Graham, E. MacKenzie, P. Ephraim, T. Travison and R. Brookmeyer, "Estimating the prevalence of limb loss in the United States: 2005 to 2050", *Archives of Physical Medicine and Rehabilitation*, vol. 89, no. 3, pp. 422-429, 2008.
- [4] M. Kiernan, S. Vucic, B. Cheah, M. Turner, A. Eisen, O. Hardiman, J. Burrell and M. Zoing, "Amyotrophic lateral sclerosis", *The Lancet*, vol. 377, pp. 942-955, 2011.
- [5] A. Schoenfeld, B. McCriskin, M. Hsiao and R. Burks, "Incidence and epidemiology of spinal cord injury within a closed American population: the United States military (2000–2009)", *Spinal Cord*, vol. 49, no. 8, pp. 874-879, 2011.
- [6] N. Peterson, D. Pisoni and R. Miyamoto, "Cochlear implants and spoken language processing abilities: review and assessment of the literature", *Restorative Neurology and Neuroscience*, vol. 28, pp. 237-250, 2010.
- [7] M. Humayun, J. Dorn, L. da Cruz, G. Dagnelie, J. Sahel, P. Stanga, A. Cideciyan, J. Duncan, D. Elliott, E. Filley, A. Ho, A. Santos, A. Safran, A. Ardit, L. Del Priore and R. Greenberg, "Interim results from the international trial of Second Sight's visual prosthesis", *Ophthalmology*, vol. 119, no. 4, pp. 779-788, 2012.
- [8] L. Hochberg, D. Bacher, B. Jarosiewicz, N. Masse, J. Simmeral, J. Vogel, S. Haddadin, J. Liu, S. Cash, P. van der Smagt and J. Donoghue, "Reach and grasp by people with tetraplegia using a neurally controlled robotic arm", *Nature*, vol. 485, no. 7398, pp. 372-375, 2012.
- [9] T. Yanagisawa, M. Hirata, Y. Saitoh, T. Goto, H. Kishima, R. Fukuma, H. Yokoi, Y. Kamitani and T. Yoshimine, "Real-time control of a prosthetic hand using human electrocorticography signals", *J. Neurosurgery*, vol. 114, no. 6, pp. 1715-1722, 2011.
- [10] K. So, S. Dangi, A. Orsborn, M. Gastpar and J. Carmena, "Subject-specific modulation of local field potential spectral power during brain-machine interface control in primates", *J. Neural Eng.*, vol. 11, no. 2, p. 026002, 2014.

- [11] S. Stavisky, J. Kao, P. Nuyujukian, S. Ryu and K. Shenoy, "A high performing brain-machine interface driven by low-frequency local field potentials alone and together with spikes", *J. Neural Eng.*, vol. 12, no. 3, p. 036009, 2015.
- [12] C. Bouton, A. Shaikhouni, N. Annetta, M. Bockbrader, D. Friedenberg, D. Nielson, G. Sharma, P. Sederberg, B. Glenn, W. Mysiw, A. Morgan, M. Deogaonkar and A. Rezai, "Restoring cortical control of functional movement in a human with quadriplegia", *Nature*, vol. 533, no. 7602, pp. 247-250, 2016.
- [13] V. Mountcastle, J. Lynch, A. Georgopoulos, H. Sakata and C. Acuna, "Posterior parietal association cortex of the monkey: command functions for operations within extrapersonal space", *J. Neurophysiology*, vol. 38, no. 4, pp. 871-908, 1975.
- [14] A. Batista, "Reach plans in eye-centered coordinates", *Science*, vol. 285, pp. 257-260, 1999.
- [15] S. Musallam, "Cognitive control signals for neural prosthetics", *Science*, vol. 305, pp. 258-262, 2004.
- [16] J. Simmeral, S. Kim, M. Black, J. Donoghue and L. Hochberg, "Neural control of cursor trajectory and click by a human with tetraplegia 1000 days after implant of an intracortical microelectrode array", *J. Neural Eng.*, vol. 8, no. 2, p. 025027, 2011.
- [17] C. Chestek, V. Gilja, P. Nuyujukian, J. Foster, J. Fan, M. Kaufman, M. Churchland, Z. Rivera-Alvidrez, J. Cunningham, S. Ryu and K. Shenoy, "Long-term stability of neural prosthetic control signals from silicon cortical arrays in rhesus macaque motor cortex", *J. Neural Eng.*, vol. 8, no. 4, p. 045005, 2011.
- [18] J. Krüger, "Seven years of recording from monkey cortex with a chronically implanted multiple microelectrode", *Front. Neuroeng.*, 2010.
- [19] D. Xing, C. Yeh and R. Shapley, "Spatial spread of the local field potential and its laminar variation in visual cortex", *J. Neuroscience*, vol. 29, no. 37, pp. 11540-11549, 2009.
- [20] G. Kreiman, C. Hung, A. Kraskov, R. Quiroga, T. Poggio and J. DiCarlo, "Object selectivity of local field potentials and spikes in the macaque inferior temporal cortex", *Neuron*, vol. 49, no. 3, pp. 433-445, 2006.
- [21] R. Andersen, J. Burdick, S. Musallam, H. Scherberger and B. Pesaran, "Recording advances for neural prosthetics", in *Proc. 26th Annual Int. Conf. IEEE EMBS*, San Francisco, CA, pp. 5352-5355, 2004.

- [22] R. Andersen, S. Musallam and B. Pesaran, "Selecting the signals for a brain-machine interface", *Curr. Opin. Neurobiology*, vol. 14, no. 6, pp. 720-726, 2004.
- [23] M. Goodale and A. Milner, "Separate visual pathways for perception and action", *Trends in Neurosciences*, vol. 15, no. 1, pp. 20-25, 1992.
- [24] G. Orban, D. Van Essen and W. Vanduffel, "Comparative mapping of higher visual areas in monkeys and humans", *Trends in Cognitive Sciences*, vol. 8, no. 7, pp. 315-324, 2004.
- [25] E. Kandel, J. Schwartz and T. Jessell, *Principles of Neural Science*. New York: McGraw-Hill, Health Professions Division, 2000.
- [26] U. Mitzdorf, "Current source-density method and application in cat cerebral cortex: investigation of evoked potentials and EEG phenomena", *Physiological Reviews*, vol. 65, no. 1, pp. 37-100, 1985.
- [27] G. Buzsáki, *Rhythms of the Brain*. Oxford: Oxford University Press, 2006.
- [28] A. Sharott, "Local field potential, methods of recording", *Encyclopedia of Computational Neuroscience*, pp. 1-3, 2014.
- [29] N. Logothetis and B. Wandell, "Interpreting the BOLD signal", *Annual Review of Physiology*, vol. 66, no. 1, pp. 735-769, 2004.
- [30] N. Logothetis, "The neural basis of the blood-oxygen-level-dependent functional magnetic resonance imaging signal", *Philosophical Transactions of the Royal Society B: Biological Sciences*, vol. 357, no. 1424, pp. 1003-1037, 2002.
- [31] H. Scherberger, M. Jarvis and R. Andersen, "Cortical local field potential encodes movement intentions in the posterior parietal cortex", *Neuron*, vol. 46, no. 2, pp. 347-354, 2005.
- [32] M. Hagan, H. Dean and B. Pesaran, "Spike-field activity in parietal area LIP during coordinated reach and saccade movements", *J. Neurophysiology*, vol. 107, no. 5, pp. 1275-1290, 2011.
- [33] T. Zanos, P. Mineault and C. Pack, "Removal of spurious correlations between spikes and local field potentials", *J. Neurophysiology*, vol. 105, no. 1, pp. 474-486, 2010.
- [34] M. Jarvis and P. Mitra, "Sampling properties of the spectrum and coherency of sequences of action potentials", *Neural Computation*, vol. 13, no. 4, pp. 717-749, 2001.

- [35] B. Pesaran, "Spectral analysis for neural signals", Center for Neural Science, New York University, pp. 1-11, 2008.
- [36] K. Shenoy, M. Churchland, G. Santhanam, B. Yu and S. Ryu, "Influence of movement speed on plan activity in monkey pre-motor cortex and implications for high-performance neural prosthetic system design", in *Proc. 25th Annual Int. Conf. IEEE EMBS*, Cancun, Mexico, 2003, pp. 1897-1900.
- [37] J. Rickert, "Encoding of movement direction in different frequency ranges of motor cortical local field potentials", *J. Neuroscience*, vol. 25, no. 39, pp. 8815-8824, 2005.
- [38] Z. Seif and M. Daliri, "Evaluation of local field potential signals in decoding of visual attention", *Cognitive Neurodynamics*, vol. 9, no. 5, pp. 509-522, 2015.
- [39] A. Mazzoni, S. Panzeri, N. Logothetis and N. Brunel, "Encoding of naturalistic stimuli by local field potential spectra in networks of excitatory and inhibitory neurons", *PLoS Comput. Biol.*, vol. 4, no. 12, p. e1000239, 2008.
- [40] A. Brewer, J. Liu, A. Wade and B. Wandell, "Visual field maps and stimulus selectivity in human ventral occipital cortex", *Nature Neuroscience*, vol. 8, no. 8, pp. 1102-1109, 2005.
- [41] C. Pierrot-Deseilligny, S. Rivaud, B. Gaymard, R. Müri and A. Vermersch, "Cortical control of saccades", *Annals of Neurology*, vol. 37, no. 5, pp. 557-567, 1995.
- [42] R. Krauzlis, "The control of voluntary eye movements: new perspectives", *The Neuroscientist*, vol. 11, no. 2, pp. 124-137, 2005.
- [43] E. Keating, "Frontal eye field lesions impair predictive and visually-guided pursuit eye movements", *Exp. Brain Res.*, vol. 86, no. 2, 1991.
- [44] M. Missal, "Supplementary eye fields stimulation facilitates anticipatory pursuit", *J. Neurophysiology*, vol. 92, no. 2, pp. 1257-1262, 2004.
- [45] G. Schalk, K. Miller, N. Anderson, J. Wilson, M. Smyth, J. Ojemann, D. Moran, J. Wolpaw and E. Leuthardt, "Two-dimensional movement control using electrocorticographic signals in humans", *J. Neural Eng.*, vol. 5, no. 1, pp. 75-84, 2008.
- [46] F. Bremmer, C. Distler and K. Hoffmann, "Eye position effects in monkey cortex. ii. pursuit- and fixation- related activity in posterior parietal areas LIP and 7A", *J. Neurophysiology*, vol. 77, no. 2, pp. 962-977, 1997.

- [47] G. Barnes, "Cognitive processes involved in smooth pursuit eye movements", *Brain and Cognition*, vol. 68, no. 3, pp. 309-326, 2008.
- [48] D. Van Essen, C. Anderson and D. Felleman, "Information processing in the primate visual system: an integrated systems perspective", *Science*, vol. 255, no. 5043, pp. 419-423, 1992.
- [49] R. Dum and P. Strick, "The origin of corticospinal projections from the premotor areas in the frontal lobe", *J. Neuroscience*, vol. 11, no. 3, pp. 667-689, 1991.
- [50] L. McGuire and P. Sabes, "Sensory transformations and the use of multiple reference frames for reach planning", *Nature Neuroscience*, vol. 12, no. 8, pp. 1056-1061, 2009.
- [51] Y. Trotter and S. Celebrini, "Gaze direction controls response gain in primary visual-cortex neurons", *Nature*, vol. 398, pp. 239-242, 1999.
- [52] J. Gardner, E. Merriam, J. Movshon and D. Heeger, "Maps of visual space in human occipital cortex are retinotopic, not spatiotopic", *J. Neuroscience*, vol. 28, no. 15, pp. 3988-3999, 2008.
- [53] Xuan Ma, Peng Zhang, Hailong Huang and Jiping He, "A study of predicting movement intentions in various spatial reaching tasks from M1 neural activities", in *Proc. 36th Ann. Int. Conf. IEEE EMBS*, 2014.
- [54] R. Andersen, G. Essick and R. Siegel, "Neurons of area 7 activated by both visual stimuli and oculomotor behavior", *Exp. Brain Res.*, vol. 67, no. 2, 1987.
- [55] K. Sathian, L. Buxbaum, L. Cohen, J. Krakauer, C. Lang, M. Corbetta and S. Fitzpatrick, "Neurological principles and rehabilitation of action disorders: common clinical deficits", *Neurorehabilitation and Neural Repair*, vol. 25, no. 5, pp. 21S-32S, 2011.
- [56] E. Hwang, M. Hauschild, M. Wilke and R. Andersen, "Inactivation of the parietal reach region causes optic ataxia, impairing reaches but not saccades", *Neuron*, vol. 76, no. 5, pp. 1021-1029, 2012.
- [57] H. Sakata, M. Taira, A. Murata and S. Mine, "Neural mechanisms of visual guidance of hand action in the parietal cortex of the monkey", *Cerebral Cortex*, vol. 5, no. 5, pp. 429-438, 1995.
- [58] H. Sakata, M. Taira, M. Kusunoki, A. Murata, Y. Tanaka and K. Tsutsui, "Neural coding of 3D features of objects for hand action in the parietal cortex of the monkey", *Philosophical*

Transactions of the Royal Society B: Biological Sciences, vol. 353, no. 1373, pp. 1363-1373, 1998.

- [59] B. Pesaran, J. Pezaris, M. Sahani, P. Mitra and R. Andersen, "Temporal structure in neuronal activity during working memory in macaque parietal cortex", *Nat. Neurosci.*, vol. 5, no. 8, pp. 805-811, 2002.
- [60] A. Graf and R. Andersen, "Brain-machine interface for eye movements", *Proceedings of the National Academy of Sciences*, vol. 111, no. 49, pp. 17630-17635, 2014.
- [61] R. Andersen and C. Buneo, "Intentional maps in posterior parietal cortex", *Ann. Rev. Neurosci.*, vol. 25, no. 1, pp. 189-220, 2002.
- [62] R. Andersen and V. Mountcastle, "The influence of the angle of gaze upon the excitability of the light-sensitive neurons of the posterior parietal cortex", *J. Neuroscience*, vol. 3, no. 3, pp. 532-548, 1983.
- [63] T. Weyand and J. Malpeli, "Responses of neurons in primary visual cortex are modulated by eye position", *J. Neurophysiology*, vol. 69, no. 6, pp. 2258-2260, 1993.
- [64] K. Nakamura, H. Chung, M. Graziano and C. Gross, "Dynamic representation of eye position in the parieto-occipital sulcus", *J. Neurophysiology*, vol. 81, no. 5, pp. 2374-2385, 1999.
- [65] C. Connor, D. Preddie, J. Gallant and D. van Essen, "Spatial attention effects in macaque area V4", *J. Neuroscience*, vol. 17, no. 9, pp. 3201-3214, 1997.
- [66] P. Brotchie, R. Andersen, L. Snyder and S. Goodman, "Head position signals used by parietal neurons to encode locations of visual stimuli", *Nature*, vol. 375, pp. 232-235, 1995.
- [67] S. Chang, C. Papadimitriou and L. Snyder, "Using a compound gain field to compute a reach plan", *Neuron*, vol. 64, no. 5, pp. 744-755, 2009.
- [68] V. Prevosto, W. Graf and G. Ugolini, "Posterior parietal cortex areas MIP and LIP receive eye position and velocity inputs via ascending preposito-thalamo-cortical pathways", *Eur. J. Neuroscience*, vol. 30, no. 6, pp. 1151-1161, 2009.
- [69] S. Wise, D. Boussaoud, P. Johnson and R. Caminiti, "Premotor and parietal cortex: corticocortical connectivity and combinatorial computations 1", *Annu. Rev. Neurosci.*, vol. 20, no. 1, pp. 25-42, 1997.

- [70] A. Murata, L. Fadiga, V. Gallese, V. Raos and G. Rizzolatti, "Object representation in the ventral premotor cortex (area F5) of the monkey", *J. Neurophysiology*, vol. 78, pp. 2226-2230, 1997.
- [71] M. Graziano, C. Taylor and T. Moore, "Complex movements evoked by microstimulation of precentral cortex", *Neuron*, vol. 34, no. 5, pp. 841-851, 2002.
- [72] L. Fogassi, V. Gallese, L. Fadiga, G. Luppino, M. Matelli and G. Rizzolatti, "Coding of peripersonal space in inferior premotor cortex (area F4)", *J. Neurophysiology*, vol. 76, no. 1, pp. 141-157, 1996.
- [73] M. Matsumura and K. Kubota, "Cortical projection to hand-arm motor area from post-arcuate area in macaque monkeys: A histological study of retrograde transport of horseradish peroxidase", *Neuroscience Letters*, vol. 11, no. 3, pp. 241-246, 1979.
- [74] L. Moll and H. Kuypers, "Premotor cortical ablations in monkeys: contralateral changes in visually guided reaching behavior", *Science*, vol. 198, pp. 317-319, 1977.
- [75] M. Churchland and K. Shenoy, "Delay of movement caused by disruption of cortical preparatory activity", *J. Neurophysiology*, vol. 97, no. 1, pp. 348-359, 2007.
- [76] J. Messier and J. Kalaska, "Covariation of primate dorsal premotor cell activity with direction and amplitude during a memorized-delay reaching task", *J. Neurophysiology*, vol. 84, no. 1, pp. 152-165, 2000.
- [77] B. Pesaran, M. Nelson and R. Andersen, "Dorsal premotor neurons encode the relative position of the hand, eye, and goal during reach planning", *Neuron*, vol. 51, no. 1, pp. 125-134, 2006.
- [78] J. Chapin, K. Moxon, R. Markowitz and M. Nicolelis, ". Real-time control of a robot arm using simultaneously recorded neurons in the motor cortex", *Nat. Neurosci.*, vol. 2, no. 7, pp. 664-670, 1999.
- [79] M. Serruya, N. Hatsopoulos, L. Paninski, M. Fellows and J. Donoghue, "Brain-machine interface: instant neural control of a movement signal", *Nature*, vol. 416, no. 6877, pp. 141-142, 2002.
- [80] R. Andersen, E. Hwang and G. Mulliken, "Cognitive neural prosthetics", *Annual Review of Psychology*, vol. 61, no. 1, pp. 169-190, 2010.

- [81] J. Collinger, B. Wodlinger, J. Downey, W. Wang, E. Tyler-Kabara, D. Weber, A. McMorland, M. Velliste, M. Boninger and A. Schwartz, "High-performance neuroprosthetic control by an individual with tetraplegia", *The Lancet*, vol. 381, pp. 557-564, 2013.
- [82] R. Andersen, S. Musallam, J. Burdick and J. Cham, "Cognitive based neural prosthetics", in *Proc. IEEE International Conference on Robotics and Automation*, 2005.
- [83] C. Buneo, M. Jarvis, A. Batista and R. Andersen, "Direct visuomotor transformations for reaching", *Nature*, vol. 416, pp. 632-636, 2002.
- [84] M. Davare, A. Zénon, M. Desmurget and E. Olivier, "Dissociable contribution of the parietal and frontal cortex to coding movement direction and amplitude", *Frontiers in Human Neuroscience*, vol. 9, 2015.
- [85] B. Pesaran, S. Musallam and R. Andersen, "Cognitive neural prosthetics", *Current Biology*, vol. 16, no. 3, pp. R77-R80, 2006.
- [86] L. Sugrue, "Matching behavior and the representation of value in the parietal cortex", *Science*, vol. 304, pp. 1782-1787, 2004.
- [87] Z. Li, "Decoding methods for neural prostheses: where have we reached?", *Front. Syst. Neurosci.*, vol. 8, 2014.
- [88] K. Shenoy and J. Carmena, "Combining decoder design and neural adaptation in brain-machine interfaces", *Neuron*, vol. 84, no. 4, pp. 665-680, 2014.
- [89] R. Faragher, "Understanding the basis of the Kalman filter via a simple and intuitive derivation [Lecture Notes]", *IEEE Signal Process. Mag.*, vol. 29, no. 5, pp. 128-132, 2012.
- [90] G. Mulliken, S. Musallam and R. Andersen, "Decoding trajectories from posterior parietal cortex ensembles", *J. Neuroscience*, vol. 28, no. 48, pp. 12913-12926, 2008.
- [91] N. Freidman, "Simultaneous decoding of reach target and eye position in premotor areas", *McGill University Master's Thesis*, 2014.
- [92] W. Wu and N. Hatsopoulos, "Real-time decoding of nonstationary neural activity in motor cortex", *IEEE Trans. Neural Syst. Rehabil. Eng.*, vol. 16, no. 3, pp. 213-222, 2008.
- [93] T. Mitchell, *Machine Learning*. New York: McGraw-Hill, 1997.

- [94] "Animals in research and teaching: research and international relations - McGill University", *Mcgill.ca*, 2016. [Online]. Available: <https://www.mcgill.ca/research/researchers/compliance/animal>. [Accessed: 01- May- 2016].
- [95] "CCAC - Canadian council on animal care: guidelines", *Ccac.ca*, 2016. [Online]. Available: http://www.ccac.ca/en/_standards/guidelines. [Accessed: 01- May- 2016].
- [96] L. Snyder, A. Batista and R. Andersen, "Coding of intention in the posterior parietal cortex", *Nature*, vol. 386, pp. 167-170, 1997.
- [97] P. Mitra and H. Bokil, *Chronux Toolbox*. <http://chronux.org/>, 2008.
- [98] P. Mitra and H. Bokil, *Observed brain dynamics*. Oxford: Oxford University Press, 2008.
- [99] D. Menzer, H. Bokil, J. Ryou, N. Schiff, K. Purpura and P. Mitra, "Characterization of trial-to-trial fluctuations in local field potentials recorded in cerebral cortex of awake behaving macaque", *J. Neuroscience Methods*, vol. 186, no. 2, pp. 250-261, 2010.
- [100] E. Hwang and R. Andersen, "Cognitively driven brain machine control using neural signals in the parietal reach region", in *Proc. Ann. Int. Conf. IEEE EMBS*, Buenos Aires, 2010.
- [101] M. Larson, "Analysis of variance", *Circulation*, vol. 117, no. 1, pp. 115-121, 2008.
- [102] A. Gelman, "Analysis of variance: why it is more important than ever", *Ann. Statist.*, vol. 33, no. 1, pp. 1-53, 2005.
- [103] "One-way ANOVA - MATLAB & simulink", *Mathworks.com*, 2016. [Online]. Available: <http://www.mathworks.com/help/stats/one-way-anova.html>. [Accessed: 01- May- 2016].
- [104] E. Schmider, M. Ziegler, E. Danay, L. Beyer and M. Bühner, "Is it really robust?", *Methodology*, vol. 6, no. 4, pp. 147-151, 2010.
- [105] G. Glass, P. Peckham and J. Sanders, "Consequences of failure to meet assumptions underlying the fixed effects analyses of variance and covariance", *Rev. Educational Research*, vol. 42, no. 3, pp. 237-288, 1972.
- [106] "F distribution", *Itl.nist.gov*, 2016. [Online]. Available: <http://www.itl.nist.gov/div898/handbook/eda/section3/eda3665.htm>. [Accessed: 01- May- 2016].
- [107] "Naive Bayes classifier - MATLAB", *Mathworks.com*, 2016. [Online]. Available: <http://www.mathworks.com/help/stats/naiivebayes-class.html>. [Accessed: 01- May- 2016].

- [108] A. Davison and D. Hinkley, *Bootstrap methods and their application*. Cambridge: Cambridge University Press, 1997, p. 194.
- [109] P. Gaspar, J. Carbonell and J. Oliveira, "On the parameter optimization of support vector machines for binary classification", *J. Integrative Bioinformatics*, vol. 9, no. 3, pp. 201-211, 2012.
- [110] C. Cortes and V. Vapnik, "Support-vector networks", *Machine Learning*, vol. 20, pp. 273-297, 1995.
- [111] C. Bishop, *Pattern recognition and machine learning*. New York: Springer, 2006, pp. 59-62.
- [112] M. Aizerman, E. Braverman and L. Rozonoer, "Theoretical foundations of the potential function method in pattern recognition learning", *Automation and Remote Control*, vol. 25, pp. 821-837, 1964.
- [113] "Train binary support vector machine classifier - MATLAB fitcsvm", *Mathworks.com*, 2016. [Online]. Available: <http://www.mathworks.com/help/stats/fitcsvm.html>. [Accessed: 01-May- 2016].
- [114] Flinders University, "Evaluation: from precision, recall and F-factor to ROC, informedness, markedness and correlation", Adelaide, AUS, 2007.
- [115] E. Astrand, P. Enel, G. Ibos, P. Dominey, P. Baraduc and S. Ben Hamed, "Comparison of classifiers for decoding sensory and cognitive information from prefrontal neuronal populations", *PLoS ONE*, vol. 9, no. 1, p. e86314, 2014.
- [116] E. Subasi, B. Townsend and H. Scherberger, "In search of more robust decoding algorithms for neural prostheses, a data driven approach", in *32nd Ann. Int. Conf. IEEE EMBS*, Buenos Aires, Argentina, 2010, pp. 4172-4175.
- [117] D. Markowitz, Y. Wong, C. Gray and B. Pesaran, "Optimizing the decoding of movement goals from local field potentials in macaque cortex", *J. Neuroscience*, vol. 31, no. 50, pp. 18412-18422, 2011.
- [118] R. Kelly, M. Smith, R. Kass and T. Lee, "Local field potentials indicate network state and account for neuronal response variability", *J. Computational Neuroscience*, vol. 29, no. 3, pp. 567-579, 2010.

- [119] E. Hwang and R. Andersen, "Brain control of movement execution onset using local field potentials in posterior parietal cortex", *J. Neuroscience*, vol. 29, no. 45, pp. 14363-14370, 2009.
- [120] S. Ohmae, T. Takahashi, X. Lu, Y. Nishimori, Y. Kodaka, I. Takashima and S. Kitazawa, "Decoding the timing and target locations of saccadic eye movements from neuronal activity in macaque oculomotor areas", *J. Neural Eng.*, vol. 12, no. 3, p. 036014, 2015.
- [121] A. Banerjee, H. Dean and B. Pesaran, "A likelihood method for computing selection times in spiking and local field potential activity", *J. Neurophysiology*, vol. 104, no. 6, pp. 3705-3720, 2010.